RECONSTRUCTING CO_2 CONCENTRATIONS IN BASALTIC MELT INCLUSIONS FROM MAFIC CINDER CONES USING RAMAN ANALYSIS OF VAPOR BUBBLES

by

ELLEN MARIE ASTER

A THESIS

Presented to the Department of Geological Sciences
and the Graduate School of the University of Oregon
in partial fulfillment of the requirements
for the degree of
Master of Science

June 2015

THESIS APPROVAL PAGE

Student: Ellen Marie Aster

Title: Reconstructing CO_2 Concentrations in Basaltic Melt Inclusions from Mafic Cinder Cones Using Raman Analysis of Vapor Bubbles

This thesis has been accepted and approved in partial fulfillment of the requirements for the Master of Science degree in the Department of Geological Sciences by:

Paul Wallace	Chairperson
James Watkins	Member
Mark Reed	Member

and

Scott L. Pratt	Dean of the Graduate School

Original approval signatures are on file with the University of Oregon Graduate School.

Degree awarded June 2015

THESIS ABSTRACT

Ellen Marie Aster

Master of Science

Department of Geological Sciences

June 2015

Title: Reconstructing CO_2 Concentrations in Basaltic Melt Inclusions from Mafic Cinder Cones Using Raman Analysis of Vapor Bubbles

Melt inclusions record valuable information about pre-eruptive melt volatile concentrations. However, a vapor bubble commonly forms in inclusions after trapping, and this decreases the dissolved CO_2 concentration in the trapped melt. To quantify CO_2 loss to bubbles, Raman spectroscopic analysis was used to determine the densities of CO_2 vapor in the bubbles. The samples analyzed in this study are from two Cascade cinder cones near Mt. Lassen and two Mexican cinder cones (Jorullo, Paricutin). Using analyses of dissolved CO_2 and H_2O in the glass in the inclusions, the measured CO_2 vapor densities were used to reconstruct the original dissolved CO_2 contents of the melt inclusions at the time of trapping. The Raman-restored CO_2 values are similar to restored CO_2 values calculated using a model of cooling and olivine crystallization in the trapped melts.

This thesis includes unpublished co-authored material.

CURRICULUM VITAE

NAME OF AUTHOR: Ellen Marie Aster

GRADUATE AND UNDERGRADUATE SCHOOLS ATTENDED:

University of Oregon, Eugene

DEGREES AWARDED:

Master of Science, Geological Sciences, 2015, University of Oregon
Bachelor of Science, Geological Sciences, 2013, University of Oregon

AREAS OF SPECIAL INTEREST:

Geochemistry
Volcanology

PROFESSIONAL EXPERIENCE:

Graduate Teaching Fellow, University of Oregon, 2013-2015

GRANTS, AWARDS, AND HONORS:

Jay McMurray Scholarship, University of Oregon, 2015
Sara J. Staggs Award, University of Oregon, 2013

PUBLICATIONS:

Chouinard, J., Donovan, J., Aster, E., Wallace, P.J. (2014) Quantitative mapping of and secondary fluorescence effects in olivine hosted melt inclusions. *Microscopy and Microanalysis* 20 Suppl. S3, 750-751.

ACKNOWLEDGMENTS

First, sincere thanks to my advisor, Paul Wallace, for supporting me throughout my Master's work. I am very grateful for his continuous, enthusiastic vision and guidance throughout this project. Also, thank you to my committee members Jim Watkins and Mark Reed for the helpful thesis edits. Also, thank you to Jim Watkins for the much-appreciated MATLAB coding assistance. Additionally, I must thank Lowell Moore, Bob Bodnar, Esteban Gazel, and Charles Farleigh for kindly "showing me the ropes" of the Raman spectrometer during my visit to Virginia Tech.

I would also like to thank my parents who are two of the most courageous and kind people I know. They imparted their enthusiasm for the natural world on me as a child, and for that I will be forever thankful. I would also like to thank my wonderful friends, Reed, and Kayak for their support and love throughout my time at the University of Oregon.

Last, thank you to the Department of Geological Sciences for the support during both my undergraduate and graduate degrees! Thank you for funding your graduate students so well, and especially for funding my travel to the 2014 American Geophysical Union meeting and Virginia Tech.

TABLE OF CONTENTS

Chapter Page

I. INTRODUCTION 1

II. METHODS 4

Sample Description and Preparation 4

Raman Spectroscopy 6

Fourier Transform Infrared (FTIR) Spectroscopy 7

Electron Microprobe Analysis 12

III. RESULTS 16

Host Olivine and Melt MgO Compositions 16

Post-entrapment Crystallization and Fe-loss Corrections 17

Raman CO_2 Densities 17

H_2O and CO_2 Concentrations 19

IV. DISCUSSION 22

Post-entrapment Formation of Vapor Bubbles 22

Restoration of Melt Inclusion CO_2 Concentrations Using CO_2 Densities 26

Reconstruction of Melt Inclusion CO_2 Concentrations Using a Cooling and Crystallization Model 27

Comparison of Raman and Bubble Formation Model Results 32

Hydrogen Loss and H_2O Reconstructions 34

Melt Inclusion Trapping Pressures 35

V. CONCLUSION 38

Chapter Page

APPENDICES 40

A. BUBBLE VOLUME CALCULATIONS 40

B. FTIR THICKNESS MEASUREMENTS AND OLIVINE INTERFERENCE CORRECTIONS 43

C. DETAILED MAXIMUM BUBBLE PERCENT CALCULATIONS 46

D. MELT INCLUSION VOLUME VERSUS BUBBLE VOLUME 54

E. COMPUTER CODE USED TO CALCULATE TIMESCALES OF CO_2 AND H_2O DIFFUSION IN BASALTIC MELT INCLUSIONS 55

REFERENCES CITED.. 63

LIST OF FIGURES

Figure Page

1. Melt inclusions corrected for post-entrapment crystallization of olivine and Fe-loss 18

2. A comparison of the total melt inclusion volume that is a vapor bubble to the measured vapor bubble CO_2 density 20

3. The result of maximum bubble volume calculations: Relationship between ΔT, the difference between formation and eruption temperatures, and the maximum percent bubble volume formed as a result of cooling and crystallization for each volcano 25

4. Percent initial CO_2 dissolved in the melt inclusion that was lost to the bubble plotted against restored melt inclusion CO_2 concentrations 27

5. A comparison of the volume percent bubble and the Raman-measured bubble CO_2 density for melt inclusions too small to analyze by FTIR 28

6. Percent re-equilibration of CO_2 between melt and vapor bubble, as calculated with MATLAB model 31

7. Comparison of melt inclusion CO_2 values restored by the model method and melt inclusion CO_2 values restored by measuring CO_2 density in the bubble with the Raman spectrometer and then adding that CO_2 back into the glass 33

8. Amount of initial dissolved H_2O that may have been lost by post-entrapment diffusive H^+ loss versus the size of the bubble as a percentage of the total melt inclusion volume 36

9. Pressure reconstructions using analyzed CO_2 and H_2O concentrations, corrected CO_2 and analyzed H_2O concentrations, and corrected CO_2 and corrected H_2O concentrations 37

LIST OF TABLES

Table Page

1. Volume percent bubbles and Raman-measured CO_2 densities 8

2. Electron microprobe and FTIR analyses of melt inclusions and major elements and volatiles in melt inclusions, uncorrected and corrected for post-entrapment crystallization and Fe-loss 13

CHAPTER I

INTRODUCTION

Melt inclusions are small volumes of melt trapped within a crystallizing phenocryst. Because melt inclusions sequester silicate melt prior to eruptive degassing, they are useful recorders of melt volatile concentrations during crystallization (e.g. Lowenstern, 1995; Metrich and Wallace, 2008). However, during post-entrapment cooling and crystallization, the pressure within a melt inclusion decreases. This causes nucleation of a vapor bubble and loss of volatiles from the melt into the bubble. The pressure drop within a melt inclusion has a particularly strong effect on CO_2 because of its strongly pressure-dependent solubility in silicate melts.

There are several factors that contribute to the post-entrapment pressure drop within a melt inclusion. First, cooling causes crystallization of the included melt along the inclusion-host interface (Steele-MacInnis et al., 2011). Because the phase transition from silicate melt to solid (e.g., olivine) results in a volume decrease, this post-entrapment crystallization causes a pressure drop within a melt inclusion, leading to nucleation of a vapor bubble (Lowenstern, 1995; Danyushevsky et al., 2002). Second, the cooling that causes crystallization also causes the melt to contract more than the olivine host because of the difference in thermal expansivity of the two phases (Sorby, 1858; Roedder, 1979). During eruption, rapid cooling from the pre-eruptive temperature to quenching at the glass transition temperature causes additional contraction of the melt. However, this may occur on too short a timescale for additional olivine crystallization along the inclusion-host interface (Anderson and Brown, 1993; Wallace et al., 2015). This process further increases vapor bubble volume. Third, diffusive loss of H^+ (protons) out of a melt inclusion (Hauri, 2001; Gaetani et al, 2012; Bucholz et al., 2013) could also increase the bubble size because this process causes an increase in melt density and a decrease in melt mass. These post-entrapment processes can strongly decrease the dissolved CO_2 concentration in a melt inclusion, making it difficult to infer the original crystallization pressure of the host crystal based on vapor saturation calculations involving H_2O and CO_2.

To investigate the extent of CO_2 loss as a result of vapor bubble formation for melt inclusions in olivine from mafic cinder cones in volcanic arcs, we employed a combination of analytical and modeling techniques. Following the methods of Moore et al. (2015), we used Raman spectroscopy to measure the CO_2 gas density in bubbles in melt inclusions from four cinder cones: two from the southern Cascade Arc (Basalt of Round Valley Butte [BRVB]; Basalt of Old Railroad Grade [BORG]) (Clynne and Muffler, 2010) and two historically active cinder cones from Mexico (Jorullo; Paricutin). We used bubble volumes, bubble CO_2 densities, and CO_2 concentrations in melt inclusion glasses (measured by Fourier transform infrared spectroscopy [FTIR]) to add the CO_2 that was lost to the bubble back into the melt of the melt inclusion (Steele-MacInnis et al., 2011; Moore et al., 2015). To distinguish bubbles co-entrapped with melt from bubbles that formed post-entrapment, we calculated a maximum bubble size for each volcano based on differences between eruptive and trapping temperatures for the melt inclusions (Riker, 2005; Wallace et al., 2015). We compared Raman-reconstructed CO_2 concentrations to CO_2 reconstructions calculated using a model of post-entrapment crystallization and melt contraction to assess the agreement between the two approaches.

Using these results together with estimates of the extent of diffusive H^+ loss, we reconstructed pressures of entrapment for melt inclusions from each volcano.

Our results show that 30 – 99% of the initial CO_2 dissolved in melt inclusions can be lost to vapor bubbles, which is similar to values by Moore et al. (2015) and Wallace et al. (2015). The estimated original trapping pressures for melt inclusions with restored CO_2 concentrations and H_2O concentrations corrected for H^+ loss are in most cases substantially higher (by ~300-4000 bars) than pressures calculated using the analyzed dissolved concentrations of H_2O and CO_2. We also used a numerical model of volatile diffusion in basaltic melt to estimate the timescales needed for melt in a melt inclusion to fully equilibrate with the bubble following a pressure drop. The model results show that equilibrium is reached during slow pre-eruptive cooling but likely not reached during rapid eruptive cooling and quenching.

The methods for analyzing CO_2 density in melt inclusion vapor bubbles via Raman spectroscopy have been developed by my coauthors Lowell Moore, Bob Bodnar, and Esteban Gazel at Virginia Tech. Lowell, Bob, and Esteban also taught me how to conduct the Raman analyses at Virginia Tech as well helped with data interpretation. Paul Wallace, my advisor at the University of Oregon and coauthor on this paper, has edited my thesis and aided with data interpretations so that the document can be submitted for publication shortly after thesis submission to the Graduate School. I collected all the data and wrote the thesis.

CHAPTER II

METHODS

Sample Description and Preparation

Olivine phenocrysts were selected from tephra samples collected by K. Walowski (BORG; BRVB) and by E. Johnson (Jorullo; Paricutin). We chose these samples to investigate differences between these four volcanoes and two different volcanic arcs, and because previous workers have conducted extensive geochemical analyses on the samples (Johnson et al., 2008; 2009; Walowski et al., 2015; in prep.). The tephra was sieved into different size fractions. The 250 µm – 500 µm and 500 µm – 1 mm fractions contained the most euhedral olivine phenocrysts with the least amount of adhering matrix glass. Phenocrysts were immersed in isopropyl alcohol and placed under a microscope for selection of olivine containing fully enclosed, glassy melt inclusions. Olivine phenocrysts were then mounted onto round glass slides using Crystalbond (an acetone-soluble adhesive). To prepare for Raman analysis, mounted samples were polished using 6 and ¼ µm diamond grit until at least one melt inclusion with a bubble was close enough (<100 µm) to the surface to be analyzed by Raman spectroscopy, but not intersected.

Olivine from BORG contain only a few mineral inclusions and usually more than one ellipsoidal melt inclusion per crystal. Most of the smooth-walled melt inclusions in BORG olivine are colorless with only a few transparent light brown inclusions. Of the 249 bubbles analyzed on the Raman spectrometer, 19 bubbles are in melt inclusions with a ‘wrinkled’ texture. The rest of the analyses were of bubbles in smooth-walled inclusions. The melt inclusions in BORG olivine also have bubbles occupying smaller volume fractions of the inclusions than are found in the other samples; bubble volumes range from 0.9–6.7% (avg. 2.9%) of the total melt inclusion volume.

BRVB olivine contain numerous mineral inclusions as well as many ellipsoidal to euhedral (negative crystal shape) melt inclusions. The melt inclusions all have smooth walls and are transparent tan in color. Eleven of the 143 bubbles analyzed on the Raman spectrometer are in melt inclusions with a small daughter crystal; the rest of the analyzed bubbles do not have daughter crystals. BRVB bubble volumes range from 1.3–13% bubble (avg. 4.1%).

Jorullo olivine also contain numerous mineral inclusions and melt inclusions are typically more euhedral (negative crystal shape) than ellipsoidal. These melt inclusions are also smooth-walled, with colors ranging from colorless to transparent tan. Four of the 81 analyzed bubbles are in melt inclusions that contain minute daughter crystals either within the melt inclusion glass or along the inclusion-host interface. The rest of the analyzed bubbles do not have daughter crystals in the melt inclusions. Jorullo melt inclusions have the largest bubble volumes ranging from 3.9–9.8% bubble (avg. 6.6%).

Paricutin olivine contain many round to euhedral (negative crystal shape) melt inclusions and reentrants. There are also numerous mineral inclusions in the olivine, and melt inclusions are typically larger compared to melt inclusions from the other three volcanoes. Of the 54 bubbles we analyzed on the Raman spectrometer from Paricutin, four are in inclusions that contain small daughter crystals. Also, four melt inclusions contain more than one bubble; however, during Raman analysis, no CO_2 was detected in any of these multiple bubbles. For Paricutin, bubble volume percent ranges from 1.7–7.5% bubble (avg. 4.2%).

Raman Spectroscopy

The density of CO_2 in vapor bubbles in melt inclusions was determined at Virginia Tech on a JY Horiba LabRam HR (800) Raman spectrometer (see Espisoto et al., 2011, and Moore et al., 2015). The Raman spectrometer was equipped with a 400-µm diameter confocal hole and a 150-µm slit. The instrument uses a Mode-Laser 514 argon laser set at 50 mW, with Raman shifted photons diffracted by an 1800 grooves/mm grating to an Andor electronically cooled CCD detector. A synthetic vapor inclusion (R. Bodnar, unpublished data) and a vapor bubble in a melt inclusion from BRVB were analyzed three times a day to calculate error from machine drift. The melt inclusion bubbles, in both the samples as well as the standards, were analyzed five times for 30 seconds; a final spectrum for each bubble was obtained from an average of these intervals. The background for each sample was corrected for noise using LabSpec software, and peaks were detected using a mixed Gaussian/Lorentzian peak fitting routine in Grams/AI. Specta containing CO_2 peaks that are too small to be detected with certainty by the peak fitting software were noted but not included in the final dataset.

The density of CO_2 in each bubble was measured using the difference in wavenumber between two characteristic peaks, called the Fermi diad, located around 1285.4 cm^{-1} and 1388.2 cm^{-1} (Wright and Wang, 1973; 1975). As CO_2 density increases, the peaks of the Fermi diad shift farther apart. The density of CO_2 can be calculated using

$$\rho_{CO_2} = -0.0303\Delta^3 + 9.43\Delta^2 - 977.398\Delta + 33780.382$$

where ρ_{CO_2} is the density of CO_2 (g/cm^3) and Δ is the difference in wavenumber (cm^{-1}) between the two peaks in the Fermi diad (Fall et al., 2011). In some melt inclusions carbonate crystals are present along the bubble-inclusion wall (e.g., Moore et al., 2015). These crystals produce a peak in Raman spectra around 1100 cm^{-1}.

To convert calculated CO_2 densities to mass CO_2 and to calculate the percentage of a given melt inclusion volume that is occupied by the vapor bubble, the volumes of the bubble and the melt inclusion must be determined (Moore et al., 2015). Using a photo of each melt inclusion and the open-source program ImageJ (Abramoff et al., 2004), we measured the dimensions of melt inclusions and bubbles and calculated a spherical volume for each bubble and an ellipsoidal volume for each melt inclusion (see Appendix A for detailed bubble volume calculations). For each ellipsoidal melt inclusion volume, we assumed that the third, unobservable ellipsoidal axis (extending in and out of the plane of each photo) was best estimated using the smaller ellipsoidal axis measured on the photograph. Bubble volumes and measured CO_2 densities are reported in Table 1, and bubbles with carbonate present are also noted.

Fourier Transform Infrared (FTIR) Spectroscopy

After the bubbles were analyzed by Raman spectroscopy, melt inclusions were prepared for analysis of glass H_2O and CO_2 concentrations using a Thermo Nicolet Nexus 670 Fourier transform infrared (FTIR) spectrometer at the University of Oregon. Each olivine grain was ground and polished using 6 and ¼ µm diamond grit into a wafer so that melt inclusions were intersected on two sides. Olivine wafer thicknesses were measured using a digital micrometer and by using interference fringes in reflectance spectra (Wysoczanski & Tani, 2007). Some melt inclusions, due to fragility of the thin wafer and their small (<30 µm in diameter) size, were not doubly intersected. For these melt inclusions, measured thicknesses were corrected for the presence of olivine (Nichols

& Wysoczanski, 2007; see Appendix B for detailed thickness measurements and calculations).

Three transmission spectra were collected from each melt inclusion glass. H_2O and CO_2 concentrations were then calculated from each spectrum using Beer's Law:

$$c = MA/\rho d\varepsilon$$

where c is the concentration of H_2O or CO_2 (in weight fraction), M is the molecular weight of H_2O or CO_2, A is the measured absorbance for total H_2O using the fundamental O-H stretching vibration (peak at 3550 cm^{-1}), or carbonate (doublet at 1515 and 1430 cm^{-1}); ρ is the glass density (kg/m^3); d is the thickness of the melt inclusion (μm); and ε is the molar absorption coefficient. For all volcanoes, ε_{H_2O} = 63 L/mol cm (Dixon et al.,

Table 1 Volume percent bubbles and Raman-measured CO_2 densities. Bubble size (expressed as a percent volume of total melt inclusion volume, or "Vol.%"), 1σ standard deviation for bubble volume percent calculations, and CO_2 density for each Raman-analyzed vapor bubble with quantifiable CO_2. The error for CO_2 density is 2.55% RSD; we estimated error for CO_2 density measurements using the deviation in CO_2 densities from repeated Raman analyses of a vapor bubble in a BRVB inclusion, as described in the text. Bubbles with carbonate are denoted with a superscript "c," and samples from which we obtained H_2O and CO_2 FTIR glass concentrations are denoted with a superscript "f."

BORG Sample	Vol.%	Vol.% S.D. (1 σ)	CO_2 Density (g/cm^3)
2.2	5.71	0.08	0.17
2.3	5.15	0.16	0.18
3.2^{c}	3.14	0.23	0.10
3.3^{c}	2.65	0.14	0.07
3.4^{c}	6.68	1.24	0.07
$5.2^{c,f}$	1.48	0.06	0.16
6.2^{f}	1.35	0.01	0.15
6.3	0.87	0.05	0.14
6.4^{c}	1.37	0.09	0.14
6.5^{c}	1.61	0.13	0.24

Table 1 (cont.)

Sample	Vol.%	Vol.% S.D. (1 σ)	CO_2 Density (g/cm^3)
9.3[c]	2.33	0.11	0.11
9.4[c]	6.08	0.57	0.12
10.2[f]	1.70	0.04	0.23
10.3	3.44	0.21	0.05
11.2[c]	6.67	0.19	0.10
12.2[c]	1.71	0.06	0.14
12.3[c]	1.18	0.06	0.14
12.4[c]	1.26	0.09	0.13
12.5[c]	1.82	0.06	0.14
13.2[f]	1.58	0.01	0.14
15.2[c]	2.78	0.14	0.14
15.d[c]	2.96	0.31	0.12
15.h[c]	3.65	0.95	0.11
18.1[c]	1.45	0.26	0.12
19.2[c,f]	1.84	0.33	0.13
19.4	3.95	0.65	0.17
19.5[f]	2.68	0.22	0.13
19.8[c,f]	1.78	0.01	0.14
19.h	4.40	0.54	0.14
19.i	3.66	0.10	0.14
19.l[c]	3.08	0.83	0.12
19.n	2.90	0.90	0.13
19.s[c]	3.64	0.83	0.15
20.1[c]	2.66	0.23	0.13
21.2[c]	1.76	0.06	0.16
23.1[f]	2.41	0.23	0.13
24.1[f]	2.42	0.30	0.17
26.1[c]	1.98	0.05	0.10
26.4	1.44	0.03	0.11
26.b[c]	2.42	0.63	0.08
27.2[f]	3.90	0.62	0.14
27.3[c]	2.25	0.01	0.16
27.b	4.01	0.75	0.14
27.c	3.81	0.17	0.16
30.a	2.61	0.17	0.22
32.a[f]	5.67	0.51	0.14
33.3[c,f]	3.42	0.29	0.14

Table 1 (cont.)

BRVB

Sample	Vol.%	Vol.% S.D. (1 σ)	CO_2 Density (g/cm^3)
2.2	4.52	0.39	0.13
2.3	3.27	0.03	0.13
2.7[c]	4.55	0.36	0.10
4.4	7.38	0.13	0.19
4.6	4.18	0.01	0.20
4.7	4.31	0.58	0.21
4.8	6.53	0.09	0.11
4.9	6.75	0.71	0.19
5.2	5.40	0.02	0.21
6.4[c]	1.55	0.08	0.23
6.5	3.04	0.17	0.24
6.6[c]	2.54	0.15	0.21
6.7[c]	1.40	0.09	0.20
6.8	3.67	0.13	0.23
6.9	1.85	0.31	0.27
8.2	3.66	0.34	0.15
8.4	3.30	0.37	0.24
10.3	8.04	0.53	0.13
11.2	3.61	0.40	0.10
11.3	5.13	0.26	0.13
11.4	1.84	0.09	0.12
14.3	8.77	0.47	0.23
18.3[f]	5.63	0.51	0.17
19.3	3.92	0.43	0.24
21.a	6.40	1.02	0.23
21.b	3.22	0.78	0.17
21.d	3.27	0.30	0.20
21.f	4.04	0.40	0.22
21.g	3.50	0.60	0.11
21.h	5.08	0.04	0.24
22.1	2.77	0.31	0.12
22-2	4.35	0.04	0.17
24.2[c]	1.72	0.06	0.24
27.1	3.10	0.08	0.09
27.d	2.07	0.16	0.18
27.e	12.99	1.33	0.16
29.a	3.50	0.51	0.09
29.b	7.02	0.31	0.12

Table 1 (cont.)

Sample	Vol.%	Vol.% S.D. (1 σ)	CO_2 Density (g/cm^3)
30.1 [f]	6.61	0.17	0.23
30.a	8.22	0.10	0.24
36.1 [c]	2.47	0.36	0.13
37.1 [f]	3.50	0.59	0.07
40.1	1.26	0.31	0.19
Jorullo			
4.c	6.59	0.99	0.18
6.a	14.29	0.32	0.13
6.b	8.34	0.58	0.15
7.a [f]	9.83	0.88	0.14
7.d	9.97	0.54	0.08
7.f	12.65	0.21	0.12
7.h	14.84	0.75	0.12
7.l	6.24	0.20	0.18
7.m	9.15	0.75	0.15
8.1 [f]	7.93	0.51	0.20
9.1	5.71	0.62	0.21
10.1	5.64	0.81	0.18
11.c [c]	5.74	0.80	0.04
12.c	6.37	0.08	0.09
13.2	12.95	0.63	0.17
18.a [c]	6.85	0.60	0.04
20.1 [c,f]	3.89	0.01	0.05
20.a [c]	6.21	0.12	0.03
Paricutin			
3.2	2.09	0.22	0.06
3.a	3.72	0.21	0.09
4.1	4.01	0.35	0.02
7.1 [f]	3.43	0.25	0.07
8.1	7.46	0.34	0.12
10.1 [f]	1.75	0.27	0.08
15.1	4.77	0.28	0.02
15.b	6.21	0.53	0.06
15.c	8.81	0.44	0.05
17.a	8.78	0.57	0.05

1995). The value for ε_{CO_2}, however, varied depending on volcano: ε_{CO_2} = 308 L/mol cm for BORG, ε_{CO_2} = 310 L/mol cm for BRVB, ε_{CO_2} = 291 L/mol cm for Jorullo and ε_{CO_2} = 280 L/mol cm for Paricutin (calculated using methods by Dixon and Pan, 1995). The absorbance of CO_2 as carbonate was calculated using a peak-fitting program that uses a background subraction of carbonate-free basaltic glass (S. Newman, unpublished). Glass densities at 1 bar and 25°C were calculated using major element concentrations as measured on the electron microprobe and partial molar volumes from R. Lange (cited in Luhr, 2001). Analytical uncertainties in CO_2 and H_2O concentrations for each melt inclusion were determined by propagating error from thickness measured by reflectance spectra, absorbance, and (for small melt inclusions) thickness after correcting for the presence of olivine in the spectra.

Electron Microprobe Analysis

Major elements in melt inclusions (Si, Al, Fe, Mg, Ca, Na, K, Mn, Ti, P) and host olivine (Si, Mg, Fe, Mn) were measured using a Cameca SX-100 electron microprobe at the University of Oregon. Five points on each melt inclusion and three points on each olivine were analyzed with a 2-µm beam diameter, 15 kV accelerating voltage, and a beam current of 20 nA.

Melt inclusion compositions were corrected for diffusive Fe loss and post-entrapment crystallization of olivine along the melt inclusion-olivine interface (Danyushevsky et al., 2000). For the correction, we used FeO^T values based on corrected melt inclusion FeO^T data [Jorullo restored FeO^T = 7.51 wt.%, Paricutin restored FeO^T = 7.18 wt.% (Johnson et al., 2009)], and whole rock data [BORG restored FeO^T = 8.54 wt.%, BRVB restored FeO^T = 9.39 wt.% (Walowski et al., 2015; in prep)]. We used

Petrolog3 (Danyushevsky and Plechov, 2011) to add equilibrium olivine incrementally back into each melt inclusion until each melt inclusion reached equilibrium with the surrounding host crystal. After restoring melt inclusion major element concentrations, we corrected for enrichments in volatiles during post entrapment crystallization. Because K is incompatible during olivine crystallization, the ratio of uncorrected K_2O to corrected K_2O for each volcano was used to correct CO_2 and H_2O values. Measured and corrected electron microprobe compositions along with measured and corrected H_2O and CO_2 concentrations for each melt inclusion are given in Table 2.

Table 2. Electron microprobe and FTIR analyses of melt inclusions and major elements and volatiles in melt inclusions, uncorrected and corrected for post-entrapment crystallization and Fe-loss. Major element values are normalized to 100% without volatiles. Major element and H_2O concentrations are expressed in wt.% and CO_2 concentrations are in ppm. H_2O and CO_2 values below FTIR detection limit are denoted "b.d." and "% ol added" is the amount of olivine added back into the melt inclusion to correct for post entrapment crystallization using Petrolog3. Error for major elements is 0.18 wt.% for Na_2O, 0.24 wt.% for SiO_2, 0.02 wt.% for K_2O, 0.18 wt.% for Al_2O_3, 0.24 wt.% for MgO, 0.12 wt.% for FeO, 0.05 wt.% for CaO, 0.01 wt.% for MnO, 0.03 wt.% for TiO_2, and 0.01 wt.% for P_2O_5. These errors were estimated using an average of electron microprobe errors from all analyses for a given oxide. Errors for H_2O and CO_2 concentrations were calculated through error propagation as detailed in the text; melt inclusions corrected for olivine interference have error shown with an asterisk. For standards, we used synthetic TiO_2 for Ti; synthetic MnO for Mn; NBS K-412 mineral glass for Al; NBS K-411 mineral glass for Fe, Ca, Si, and Mg; $Ca_{10}(PO_4)_6Cl_2$ (halogen corrected) for P; nepheline for Na; and orthoclase MAD-10 for K. Time dependent intensity corrections were made for Na, K, Si and Al. Electron microprobe melt inclusion analyses that showed olivine

Uncorrected	BORG									
	5.2	19.2	19.5	19.8	22.3	23-1	24.1	27.2	32.a	33.3
SiO_2	49.46	48.18	48.51	49.85	49.31	50.35	48.46	51.21	50.88	47.66
TiO_2	0.92	0.89	0.95	0.95	0.88	1.15	0.76	0.97	0.88	0.77
Al_2O_3	20.28	21.57	21.46	20.79	19.63	19.89	19.32	20.33	19.40	20.10
FeO^T	6.05	6.52	5.96	6.43	8.47	7.58	6.57	6.54	7.22	7.82
MnO	0.09	0.12	0.08	0.10	0.13	0.12	0.10	0.12	0.12	0.13
MgO	4.06	4.34	4.63	4.90	5.61	3.74	6.95	3.28	4.50	5.75
CaO	11.59	10.00	9.99	9.93	9.56	9.39	11.47	9.98	9.32	10.64

Na_2O	3.39	4.54	4.63	4.89	3.99	4.19	3.15	4.44	4.18	3.17
K_2O	0.60	0.59	0.65	0.65	0.51	0.64	0.54	0.63	0.59	0.46
P_2O_5	0.27	0.23	0.22	0.22	0.22	0.26	0.23	0.24	0.23	0.20
H_2O	2.4	1.9	1.7	1.8	b.d.	1.3	0.9	1.7	0.9	0.7
H_2O error	±0.3*	±0.2*	±0.4*	±0.7*	N/A	±0.4*	±0.03	±0.4	±0.5	±0.03
CO_2 ppm	1141	688	559	1443	b.d.	761	320	880	b.d.	303
CO_2 error	±207*	±323*	±289*	±444*	N/A	±52*	±46	±45	N/A	±57
Uncorrected	BRVB				Jorullo		Paricutin			
	18.3	24-2	31-3	37-1	14.1	20.1	1.1	7.1	12.1	
SiO_2	47.89	48.58	48.17	47.18	49.77	49.88	52.46	51.21	51.68	
TiO_2	1.69	1.57	1.51	1.51	0.92	0.86	1.03	1.01	1.03	
Al_2O_3	19.49	17.82	18.00	19.19	20.83	19.39	19.98	20.23	19.22	
FeO^T	8.05	7.31	7.45	8.51	5.56	6.11	6.07	7.10	7.91	
MnO	0.13	0.11	0.12	0.14	0.08	0.09	0.13	0.12	0.13	
MgO	5.08	5.87	6.64	5.44	4.21	6.32	3.91	3.61	4.37	
CaO	10.68	10.74	10.37	10.24	10.08	9.57	8.36	8.45	8.09	
Na_2O	4.15	4.23	3.87	4.08	4.86	4.67	5.12	4.24	4.47	
K_2O	1.15	0.93	0.80	1.14	0.77	0.72	0.94	0.90	0.88	
P_2O_5	0.51	0.47	0.46	0.49	0.32	0.29	0.34	0.36	0.35	
H_2O	0.1	1.6	1.2	0.4	2.6	2.8	1.4	1.6	0.8	
H_2O error	±0.01	±0.8*	±0.14	±0.04	±0.17	±0.3	±0.1*	±0.3	N/A	
CO_2 ppm	608	b.d.	905	b.d.	532	654	328	794	509	
CO_2 error	±43	N/A	±150	N/A	±100	±76	±18*	±61	N/A	

Corrected	BORG									
	5.2	19.2	19.5	19.8	22.3	23.1	24.1	27.2	32.a	33.3
SiO_2	48.17	47.64	47.85	48.70	50.07	50.14	48.14	49.96	51.02	48.49
TiO_2	0.79	0.82	0.86	0.88	0.89	1.09	0.70	0.86	0.85	0.76
Al_2O_3	17.39	19.74	19.35	19.06	19.83	18.76	17.86	18.14	18.61	19.73
Fe_2O_3	0.86	0.89	0.90	0.95	0.90	0.94	0.86	0.93	0.92	0.81
FeO	7.77	7.74	7.74	7.69	7.73	7.80	7.79	7.75	7.72	7.82
MnO	0.08	0.11	0.08	0.09	0.13	0.12	0.10	0.11	0.11	0.13
MgO	9.32	7.28	7.91	7.04	6.02	6.23	9.50	7.10	6.37	7.44
CaO	9.94	9.16	9.01	9.11	9.65	8.86	10.61	8.91	8.94	10.45
Na_2O	2.91	4.16	4.17	4.48	4.04	3.95	2.91	3.96	4.02	3.11
K_2O	0.51	0.54	0.59	0.59	0.52	0.61	0.50	0.56	0.57	0.45
P_2O_5	0.23	0.21	0.20	0.20	0.22	0.24	0.22	0.22	0.22	0.20
H_2O	2.0	1.7	1.5	1.6	b.d.	1.3	0.8	1.5	0.8	0.6

CO_2 ppm	970	630	505	1322	b.d.	718	296	786	b.d.	298
Olivine (Fo%)	87.70	85.30	86.40	85.00	82.20	82.50	88.00	84.50	82.90	84.90
% ol added	16.70	9.72	11.43	8.15	0.66	7.13	8.98	11.95	5.90	4.45

Corrected	BRVB				Jorullo		Paricutin		
	18.3	24.2	31.3	37.1	14.1	20.1	1.1	7.1	12.1
SiO_2	47.67	48.21	47.95	47.47	47.98	48.30	51.61	50.88	52.13
TiO_2	1.59	1.45	1.43	1.47	0.77	0.76	0.96	0.96	1.02
Al_2O_3	18.41	16.46	16.99	18.60	17.39	17.00	18.73	19.10	19.06
Fe_2O_3	1.13	1.14	1.08	1.12	0.87	0.88	0.83	0.76	0.80
FeO	8.38	8.37	8.42	8.39	6.74	6.72	6.44	6.58	6.49
MnO	0.12	0.10	0.12	0.14	0.07	0.08	0.12	0.11	0.13
MgO	7.06	8.41	8.30	6.97	10.54	10.44	6.10	6.50	5.89
CaO	10.09	9.92	9.79	9.92	8.41	8.40	7.84	7.98	8.03
Na_2O	3.92	3.91	3.65	3.96	4.06	4.10	4.80	4.00	4.43
K_2O	1.09	0.86	0.76	1.11	0.64	0.63	0.88	0.85	0.87
P_2O_5	0.48	0.43	0.43	0.47	0.27	0.25	0.32	0.34	0.35
H_2O	0.1	1.5	1.1	0.4	2.2	2.4	1.3	1.5	0.8
CO_2 ppm	574	b.d.	854	b.d.	444	573	307	750	504
Olivine (Fo%)	83.90	86.10	85.70	83.70	90.80	90.70	85.40	85.60	84.60
% ol added	6.54	9.09	6.67	4.60	18.75	12.54	6.51	6.73	2.26

CHAPTER III

RESULTS

Host Olivine and Melt MgO Compositions

BORG olivine compositions are $Fo_{82.2}$–Fo_{88} (avg. $Fo_{84.9}$). BRVB olivine are similar, with an average of $Fo_{84.9}$ and with a range of $Fo_{83.7}$–$Fo_{86.1}$. For Paricutin, three analyzed olivine grains have an average of $Fo_{85.2}$, with a range of $Fo_{84.6}$–$Fo_{85.6}$. These Fo contents for Paricutin are on the low end of the range of Fo contents reported in Johnson et al. (2009). Jorullo olivine have the most Fo-rich composition. The two Jorullo olivine analyzed in this study have olivine compositions of $Fo_{90.7}$ and $Fo_{90.8}$. These values are comparable to host forsterite contents from the same Jorullo tephra sample as analyzed by Johnson et al. (2008).

Uncorrected ranges in MgO contents for BORG melt inclusions are 3.28–6.95 wt.% (avg. 4.78 wt.%), with concentrations corrected for post entrapment crystallization and Fe loss ranging 6.02–9.50 wt.% MgO (avg. 7.42 wt.%). Analyzed compositions for BRVB melt inclusions are slightly more mafic, with MgO concentrations ranging from 5.08–6.64 wt.% MgO (avg. 5.75 wt.%). Corrected compositions for BRVB have MgO concentrations ranging from 6.97–8.41 wt.% (7.68 wt.%). Although only two inclusions were analyzed from Jorullo, MgO corrected and uncorrected concentrations are similar to those observed in Johnson et al. (2008). Uncorrected MgO concentrations are 4.21 wt.% and 6.32 wt.%, with corrected concentrations of 10.44 wt.% and 10.54 wt.%. The MgO concentrations from the three Paricutin inclusions analyzed in this study range from 3.61–4.37 wt.% (avg. 3.96 wt.%), with corrected concentrations of 5.89–6.50 wt.% (avg.

6.16 wt.%). These are also within the ranges of measured and corrected concentrations observed in Johnson et al. (2009).

Post-entrapment Crystallization and Fe-loss Corrections

The melt inclusions from each volcano experienced variable extents of post-entrapment crystallization and Fe loss (Fig. 1). On average, Jorullo melt inclusions had the greatest amount of post-entrapment crystallization (avg. of 15.6% olivine added back into melt inclusions) whereas BRVB experienced the least (avg. of 6.7 % olivine added back into melt inclusions). On average, BORG required 8.5% olivine added back into its melt inclusions, whereas 5.2% olivine was added back into Paricutin inclusions to correct for post entrapment crystallization.

Raman CO_2 Densities

A total of 415 bubbles were analyzed by Raman spectroscopy. Out of the 143 bubbles from BRVB, 67 have detectable CO_2 (i.e., a Fermi diad is present in the Raman spectrum). After background corrections, 43 of the 67 bubbles have Fermi diad peaks that were fit with confidence using the peak fitting software and background corrections. Out of the 143 bubbles analyzed, 10 have carbonate peaks in their Raman spectra. For BORG, of 249 analyzed bubbles, 96 have Raman spectra with Fermi diads, and 47 of these were fit with reasonable certainty. Of the 249 analyzed bubbles, 55 have carbonate peaks in their Raman spectra. We analyzed 54 bubbles from Paricutin, of which 18 show Fermi diads, and 11 were fit with the peak fitting and background correction software. No

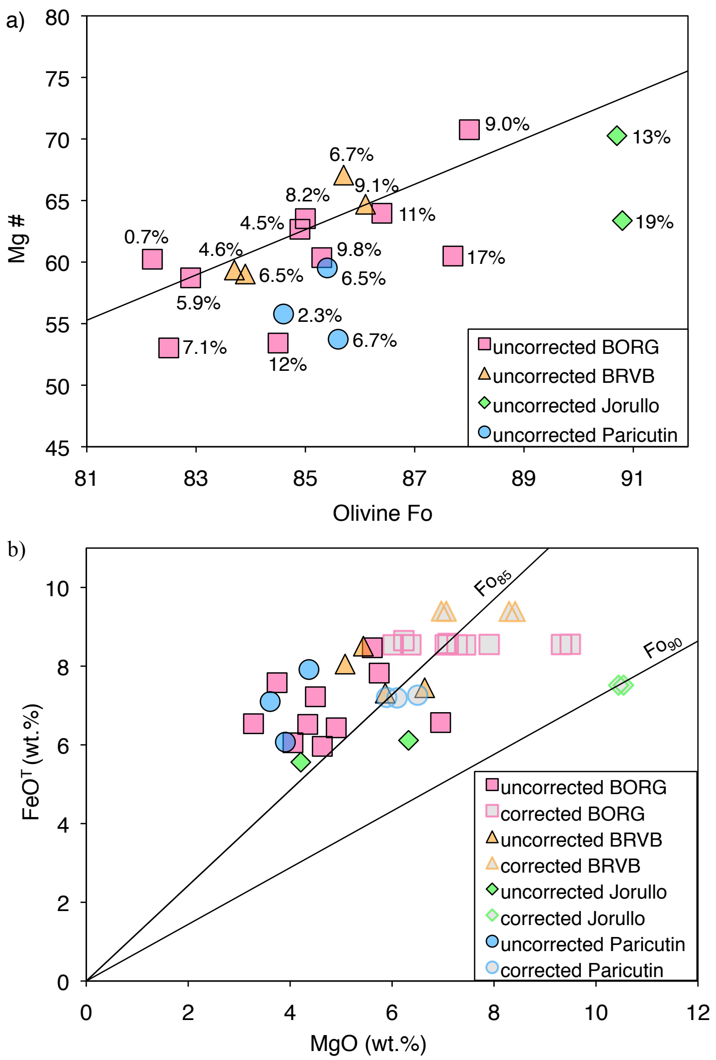

Fig. 1. Melt inclusions must be corrected for post-entrapment crystallization of olivine and Fe-loss. (a) Uncorrected Mg # [Mg # = $100(Mg^{2+}/(Mg^{2+}+Fe^{2+}))$] compared to the Fo-content of the olivine host. The black line shows the composition of melt inclusions with no post-entrapment crystallization, and percentages indicate the amount of olivine added back into each melt inclusion to restore it to a composition prior to post-entrapment crystallization. While post-entrapment crystallization will decrease Mg #, Fe-loss will increase Mg #, resulting in the observed spread of corrected values around the black line representing no post-entrapment crystallization. (b) Comparing uncorrected to corrected melt inclusion FeO^T and MgO compositions shows the narrow range of corrected FeO^T compositions. Black lines show olivine host Fo-content; melt inclusions were corrected for post-entrapment crystallization to be in equilibrium with an olivine host with a Fo-content between Fo$_{82.5}$ and Fo$_{90.8}$, depending on the sample.

analyzed bubbles from Paricutin have spectra with carbonate peaks. We analyzed 81 bubbles from Jorullo, of which 29 have detectable CO_2, and 18 could be fit. Of the 81 bubbles analyzed from Jorullo, 36 have Raman spectra with carbonate peaks.

Each volcano has a distinct array of CO_2 densities and percent bubble volumes (Fig. 2). BRVB CO_2 densities range from 0.07 to 0.29 g/cm^3 (avg. 0.17 g/cm^3). BORG has lower CO_2 densities, with values from 0.05 g/cm^3 to 0.24 g/cm^3 (avg. 0.14 g/cm^3). Paricutin melt inclusions have bubbles with the lowest recorded CO_2 densities, ranging from 0.02 g/cm^3 to 0.12 g/cm^3 (avg. 0.07 g/cm^3). Jorullo melt inclusions contain bubbles with CO_2 densities of 0.03 g/cm^3 to 0.21 g/cm^3 (avg. 0.12 g/cm^3). CO_2 densities in bubbles with detectable carbonate have similar (BRVB) or lower (Jorullo) CO_2 densities than bubbles without carbonate.

H_2O and CO_2 Concentrations

To reconstruct the original dissolved CO_2 concentrations of the melt inclusions at the time of trapping, the amount of CO_2 in the melt inclusion glass must be known. However, to measure the concentrations of H_2O and CO_2 in the glass by FTIR spectroscopy requires that the melt inclusion has a diameter larger than ~30 μm. Thus, for melt inclusions smaller than 30 μm in diameter, we estimated the amount of CO_2 and H_2O in the glass using the median CO_2 and H_2O concentration for each volcano obtained through compiling data from this study and published results (Johnson et al., 2008; 2009; Walowski et al., 2015; in prep.). For BRVB, the median H_2O concentration is 1.7 wt.% with a median CO_2 of 538 ppm. For BORG, the median H_2O concentration is 2.9 wt.% with a median CO_2 concentration of 937 ppm. For samples from Jorullo, the median H_2O concentration is 3.0 wt.% and the median CO_2 concentration is 630 ppm. And last, for

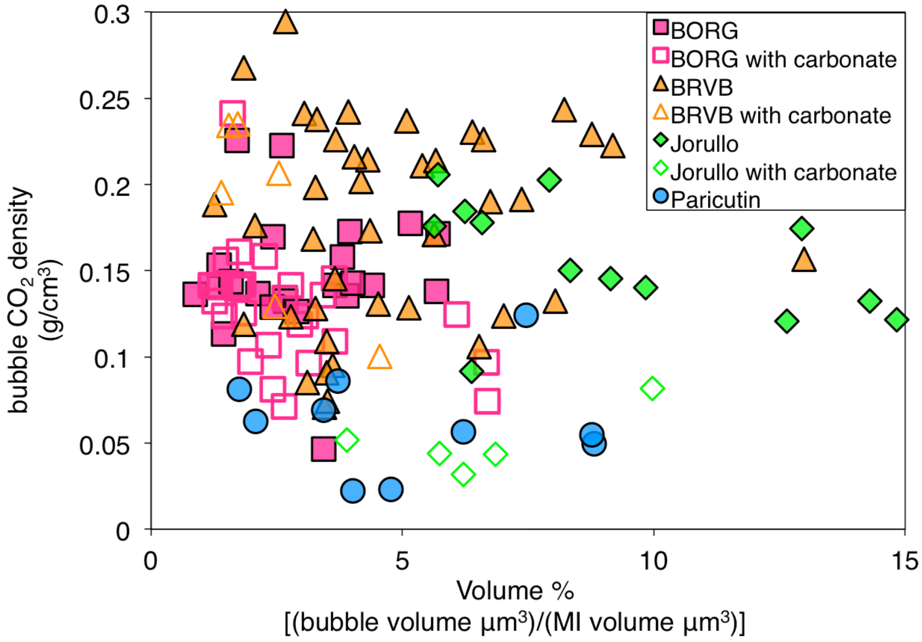

Fig. 2. A comparison of the total melt inclusion volume that is a vapor bubble (or, 'Volume %') to the measured vapor bubble CO_2 density shows that each volcano has a unique array of CO_2 densities and bubble volumes. CO_2 densities in bubbles with detectable carbonate are fairly similar (e.g. BORG) or lower (e.g. Jorullo) than CO_2 densities in bubbles without carbonate.

Paricutin, the median H_2O concentration is 4.5 wt.% and the median CO_2 concentration is 850 ppm. Again, these values are our estimates of the amount of CO_2 and H_2O in melt inclusion glasses for melt inclusions too small to analyze by FTIR, but for which we have measurable, vapor bubble CO_2 densities.

Twenty-seven inclusions from this study are large enough for FTIR analysis. For BORG, 13 analyzed melt inclusions yield CO_2 concentrations ranging from below detection (which, for the FTIR, is ~ 25 ppm) to 1443 ppm (avg. 788 ppm). BORG melt inclusion H_2O concentrations range from 0.7 to 2.1 wt.% (avg. 1.5 wt.%). For five analyzed BRVB inclusions, CO_2 concentrations range from below detection (~25 ppm) to 905 ppm (avg. 489 ppm). The H_2O concentrations for BRVB range from 0.07 to 1.6 wt.%

(avg. 0.8 wt.%). For Jorullo, three inclusions have CO_2 concentrations ranging from 532 to 897 ppm (avg. 699 ppm) with H_2O concentrations ranging from 0.6 to 2.8 wt.% (avg. 2.0 wt.%). Finally, the six FTIR-analyzed Paricutin melt inclusions have CO_2 concentrations ranging from 328 to 1136 ppm (avg. 621 ppm) with H_2O concentrations ranging from 0.8 to 1.6 wt.% (avg. 1.4 wt.%). These inclusions provide our best estimates of melt inclusion CO_2 reconstructions since both CO_2 densities in the bubble as well as CO_2 concentrations in the glass were measured.

CHAPTER IV

DISCUSSION

Post-entrapment Formation of Vapor Bubbles

The size of a vapor bubble in a melt inclusion is strongly dependent on the extent of post-entrapment crystallization and thermal contraction of the melt phase relative to the contraction of the olivine host (Riker, 2005; Moore et al., 2015; Wallace et al., 2015). However, a crystallizing phenocryst can also trap melt that already has one or more bubbles. To determine which bubbles may have formed in the melt prior to melt inclusion entrapment, we used the method of Riker (2005) to estimate the maximum bubble volume fraction that could form in melt inclusions from each volcano as a result of post-entrapment crystallization and thermal contraction. This calculation allows us to screen out melt inclusions with pre-entrapment bubbles and exclude them from our CO_2 reconstruction procedures, because these bubbles would cause an overestimate of the amount of CO_2 that was dissolved in the melt inclusion at the time of trapping.

For the bubble volume calculations, we assumed that there are two stages in the post-entrapment formation and growth of a bubble. The first stage occurs during post-entrapment cooling up to the point of eruption. It involves both olivine crystallization (which changes melt composition) and changes in the density of the included melt due to temperature decrease. The size of a bubble formed during this stage is therefore a function of ΔT, the difference between the eruption and trapping temperatures of the melt inclusion (Anderson and Brown, 1993; Riker, 2005; Wallace et al., 2015). The second stage occurs over short timescales during eruptive cooling and involves thermal contraction of the melt down to the glass transition temperature. This second stage likely occurs too rapidly to allow for any additional olivine crystallization.

To simulate the growth of a vapor bubble as a result of cooling, we first identified the most primitive melt composition (high MgO, low SiO_2) for each volcano based on analyzed inclusions from this study as well as those analyzed from the same sample suites (Johnson et al., 2009; Walowski et al., 2015; in prep.). We used the highest H_2O/K_2O ratio of melt inclusions from each cone multiplied by the K_2O content of the most primitive melt to determine H_2O for the primitive melt composition. Last, we paired the primitive melt composition with the highest measured glass CO_2 concentration. Pre-eruption and trapping temperatures (based on analyzed and restored melt inclusion compositions, respectively) for each primitive composition were taken from the Petrolog3 output.

We modeled the first stage of post-entrapment bubble formation using rhyolite-MELTS (Gualda et al., 2012; this version of MELTS has the most up-to-date calibration for all melt compositions) to simulate equilibrium crystallization of each primitive melt composition from the liquidus temperature to 140° below the liquidus temperature in increments of 20°C. For each temperature step, we used the mass and density of olivine crystallized to calculate the volume change of a melt inclusion during cooling and crystallization. We calculated the density of the residual melt at each temperature step using the method of Lange and Carmichael (1990). We also calculated the volume decrease of the cavity containing the melt inclusion caused by olivine host contraction over the 140°C interval. The volume difference between the cavity and the melt plus post-entrapment olivine crystallized at each sub-liquidus temperature step is then equal to the volume of a vapor bubble formed as a result of post-entrapment crystallization. One important result of these calculations is that during this stage of post-entrapment crystallization, the vapor bubble forms solely due to the volume change caused by crystallization of olivine from the included melt. The residual melt in the melt inclusion actually becomes less dense with decreasing temperature because of decreasing melt MgO and FeO and increasing melt H_2O caused by crystallization of olivine, and this compositional effect more than offsets the melt contraction effect due to cooling alone.

For the second (eruptive) stage of bubble expansion, we calculated the changes in melt and olivine density from the pre-eruptive temperature to the glass transition temperature, at which point we assume any further bubble expansion ceases. During this process, we assumed that the olivine and melt compositions did not change. Glass transition temperatures are dependent on H_2O content and were calculated for each temperature step using Giordano et al. (2005). Full details of the bubble calculation procedures are given in Appendix C.

The results of these calculations allow us to place an upper limit on the size of bubbles that could have formed post-entrapment. A comparison of the calculations with our sample data suggests that almost all analyzed bubbles formed as a result of post-entrapment crystallization and thermal contraction of the melt phase (Fig. 3). Melt inclusions with bubbles that are larger than the calculated maximum bubble volume

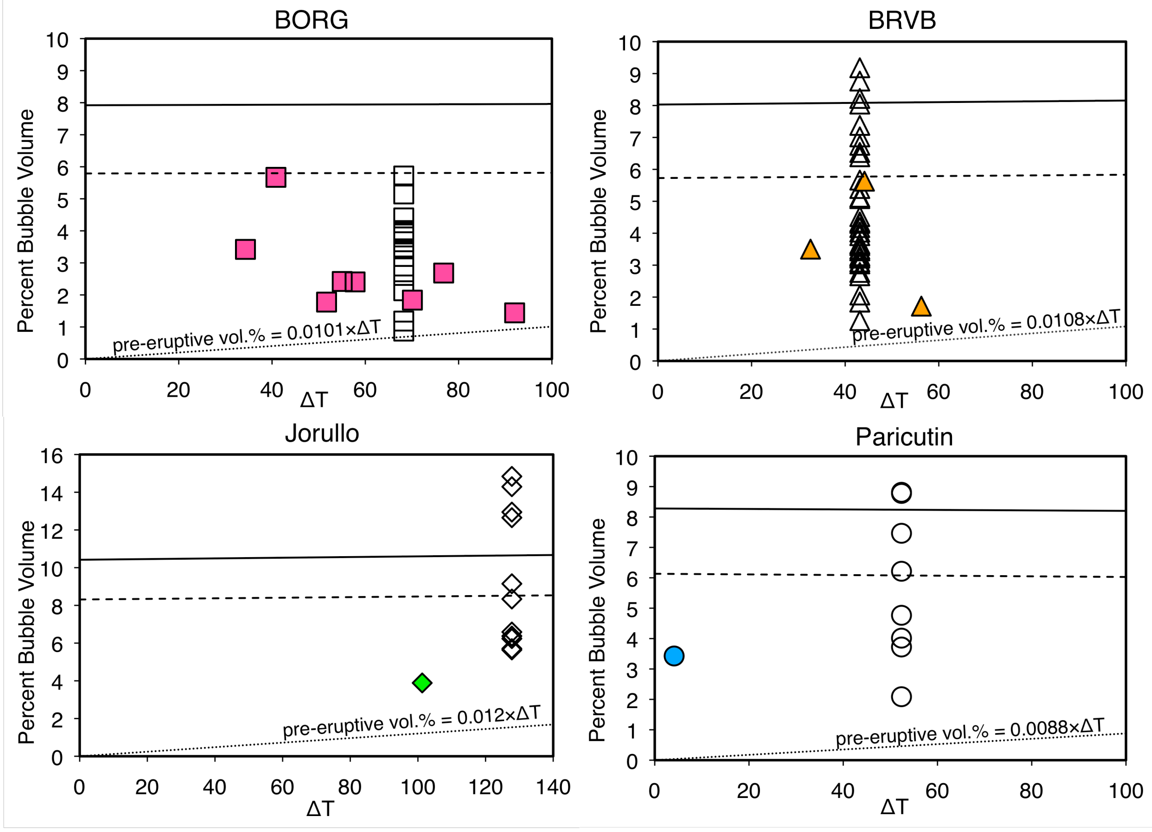

Fig. 3. These plots are the result of our maximum bubble volume calculations. They show the relationship between ΔT, the difference between formation and eruption temperatures, and the maximum percent bubble volume formed as a result of cooling and crystallization for each volcano. The dotted line represents percent bubble volume formed as a result of pre-eruptive, post-entrapment crystallization, the solid line represents percent bubble volume formed as a result of post-entrapment crystallization and thermal contraction of the melt in the melt inclusion. Finally, the dashed line shows the percent bubble volume formed as a result of post-entrapment crystallization, thermal contraction of the melt in the melt inclusion, and thermal contraction of the olivine host. Solid symbols represent bubbles in melt inclusions with electron microprobe data. Open symbols represent bubbles in melt inclusions without electron microprobe data; for these an average of the microprobe data was used to estimate ΔT. Symbols plotting above the dashed line may have formed in the melt prior to melt inclusion entrapment. Therefore, these melt inclusions and bubbles were not used in melt inclusion CO_2 reconstructions. We used the equations for pre-eruptive bubble volume percentage for the calculated (model) CO_2 reconstructions (for more information about this calculation, see text).

percent were excluded from final CO_2 reconstructions, as these are likely to be bubbles that were formed before entrapment and were then co-entrapped with melt into a melt inclusion. Comparing melt inclusion volume to bubble volume (Appendix D; Fig. D1) shows that the majority of melt inclusions for each volcano have similar volume percent bubbles. This again suggests that most of the bubbles in the melt inclusions are the result of post entrapment crystallization and thermal contraction of the melt phase instead of bubble nucleation in the melt prior to melt inclusion entrapment.

Restoration of Melt Inclusion CO_2 Concentrations Using CO_2 Densities

The CO_2 concentrations in the melt inclusions at the time of trapping (before vapor bubble formation) can be calculated using the Raman-measured CO_2 densities and the glass CO_2 concentrations. Reconstructing melt inclusion CO_2 concentrations for melt inclusions large enough to be analyzed on the FTIR suggests that 43–99% of the CO_2 originally in a melt inclusion can be lost to a vapor bubble post-entrapment (Fig. 4). These values are similar to what has been found for melt inclusions from other basaltic eruptions (Moore et al., 2015; Wallace et al., 2015). In general, the restored CO_2 does not depend on the percent CO_2 lost by post-entrapment bubble formation, though there are four melt inclusions with very high restored CO_2 that also have some of the greatest extents of CO_2 loss. For smaller inclusions that could not be analyzed by FTIR, we used the median CO_2 of other analyzed inclusions from the same cinder cone. The Raman results for the small inclusions suggest that 30–90% of initial dissolved CO_2 is contained in the bubble, comparable to the values given above for melt inclusions in which the glass CO_2 had been analyzed by FTIR (Fig. 5).

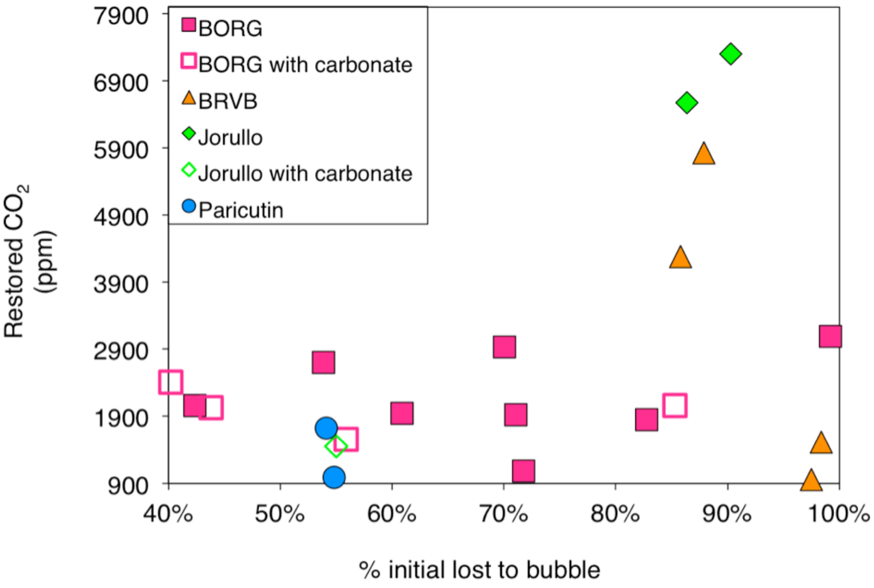

Fig. 4. The percent of initial CO_2 dissolved in the melt inclusion that was lost to the bubble plotted against restored melt inclusion CO_2 concentrations. For these inclusions, we measured both CO_2 densities in the bubble (from Raman spectrometer analysis) and CO_2 concentrations in the glass (from FTIR analysis), so these samples represent our most accurate estimates of restored melt inclusion CO_2 concentrations.

Reconstruction of Melt Inclusion CO_2 Concentrations Using a Cooling and Crystallization Model

For comparison with the CO_2 reconstructions based on the Raman data, we also estimated the original CO_2 concentrations of the melt inclusions using the results of the bubble formation model discussed above. This method is based on the approach used by Anderson and Brown (1993; see also Riker, 2005; Wallace et al., 2015). In this model, the volume fraction of the pre-eruptive bubble is estimated using the temperature difference between trapping and eruption. The composition of the vapor phase is then estimated using the solubility relations of Iacono-Marziano et al., (2012). With this information, the number of moles of CO_2 in the vapor can be calculated and then added to the measured dissolved CO_2. An important assumption in this approach is that CO_2 is

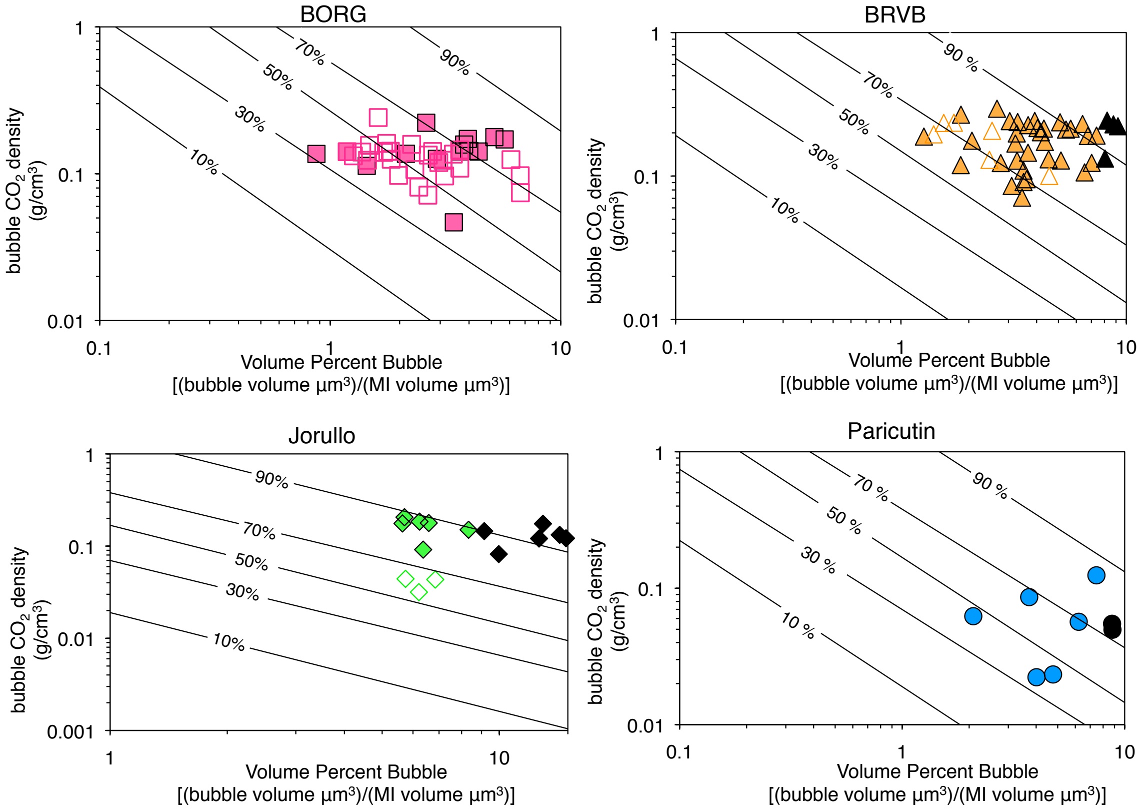

Fig. 5. A comparison of the volume percent bubble and the Raman-measured bubble CO_2 density for melt inclusions too small to analyze by FTIR (<30 µm in diameter). For these melt inclusions, the median CO_2 value of other analyzed inclusions from the same cone was used to estimate the amount of CO_2 in the glass. Black lines represent percent CO_2 originally dissolved in the melt inclusion that was lost to the vapor bubble. Open symbols represent bubbles with carbonate. Black symbols show bubbles with a volume that exceeds the maximum volume calculated for bubbles from that volcano (see "Post Entrapment Formation of Vapor Bubbles" in Discussion): These bubbles might have formed prior to melt inclusion entrapment, so they were not used in final CO_2 reconstructions. These melt inclusion CO_2 reconstructions suggest that ~30–90% of CO_2 initially dissolved in the melt is contained in the bubble.

lost from the melt to the vapor bubble only during the pre-eruptive stage because the eruptive expansion stage occurs on such short timescales that appreciable CO_2 cannot diffuse into the bubble (Wallace et al., 2015).

To test this assumption, and to explore the timescales of CO_2 and H_2O diffusion from the melt in a melt inclusion to a vapor bubble, we created a MATLAB code to model one-dimensional diffusion as a result of an isothermal, instantaneous pressure drop. With a user-specified time of diffusion, the code outputs the mass composition of the vapor in the bubble and diffusion profiles for CO_2 and H_2O from the farthest end of the melt inclusion to the melt inclusion-bubble interface.

The code uses equations formulated by Lloyd et al. (2014) for the diffusivities of H_2O and CO_2 as a function of distance from a bubble:

$$D_{H_2O} = C_{H_2O} \exp\left(-8.56 - \frac{19110}{T}\right) \times (0.057 \ln(X) + 0.0732)$$

$$D_{CO_2} = \exp\left(-13.99 - \frac{17367 + 1944.8P}{T} + \frac{855.2 + 271.2P}{T} \times C_{H_2O}\right)$$

where D_{H_2O} and D_{CO_2} are the diffusivities of H_2O and CO_2 (m^2/s), C_{H_2O} is the concentration of H_2O (wt.%), T is the temperature (K), X is the distance from the bubble (μm), and P is the pressure (GPa). Because both D_{H_2O} and D_{CO_2} depend on the concentration of H_2O, we used a diffusion equation for both H_2O and CO_2 that considered the derivative of the diffusivity as a function of distance from the bubble:

$$\frac{dC}{dt} = \frac{dD}{dx} \bullet \frac{dC}{dx} + D\frac{d^2C}{dx^2}$$

where C is the concentration, t is time, D is the diffusivity, and x is the distance from the melt inclusion-bubble interface (for further information about the code, see Appendix F).

To assess the timescale of CO_2 loss to a vapor bubble, we started with a pressure of 3000 bars and then decreased the pressure to 2000 bars (ΔP = 1000 bars) or 1000 bars (ΔP = 2000 bars) at a temperature of 1150°C. This is the pressure drop that would occur due to cooling and crystallization. The starting pressure of 3000 bars is the approximate middle range of pressures for BORG melt inclusions from this study after CO_2

reconstructions, and the ending pressures of 2000 and 1000 bars are two possible end pressures representing the range of pressures based on the actual analyzed concentrations of H_2O and CO_2 in the melt inclusion. We ran these simulations for a 40 µm diameter inclusion, the average BORG melt inclusion diameter, and a 100 µm diameter inclusion, the maximum BORG melt inclusion diameter. All runs had a 10 µm bubble (an average diameter for BORG bubbles), and a H_2O concentration of 1.5 wt.% (an approximate average analyzed H_2O concentration for BORG melt inclusions). For each of the two pressure drops, we modeled a ~30 minute (~2000 seconds) diffusion duration, until melt CO_2 was in equilibrium with the bubble. We assumed equilibrium when the first node (at the bubble-inclusion interface) and the last node (at the inclusion-crystal interface) were within ±0.01 ppm CO_2. We then ran the code over shorter timescales to assess the time dependence of CO_2 loss.

The results show that the melt and vapor reach equilibrium after ~6 minutes for a 40 µm inclusion and after ~30 minutes for a 100 µm inclusion (Fig. 6). This indicates that if post-entrapment but pre-eruption cooling and crystallization occur on timescales longer than ~6 to 30 minutes, the bubble will reach equilibrium with the melt.

As discussed above, during eruption, a bubble will expand considerably as the melt rapidly cools to the glass transition temperature. Modeling the timescale of CO_2 loss to the bubble during eruption is more complex than the case discussed above because the rapid and large change in temperature causes diffusion rates of H_2O and CO_2 to decrease by several orders of magnitude. We ran simulations of CO_2 loss to bubbles at

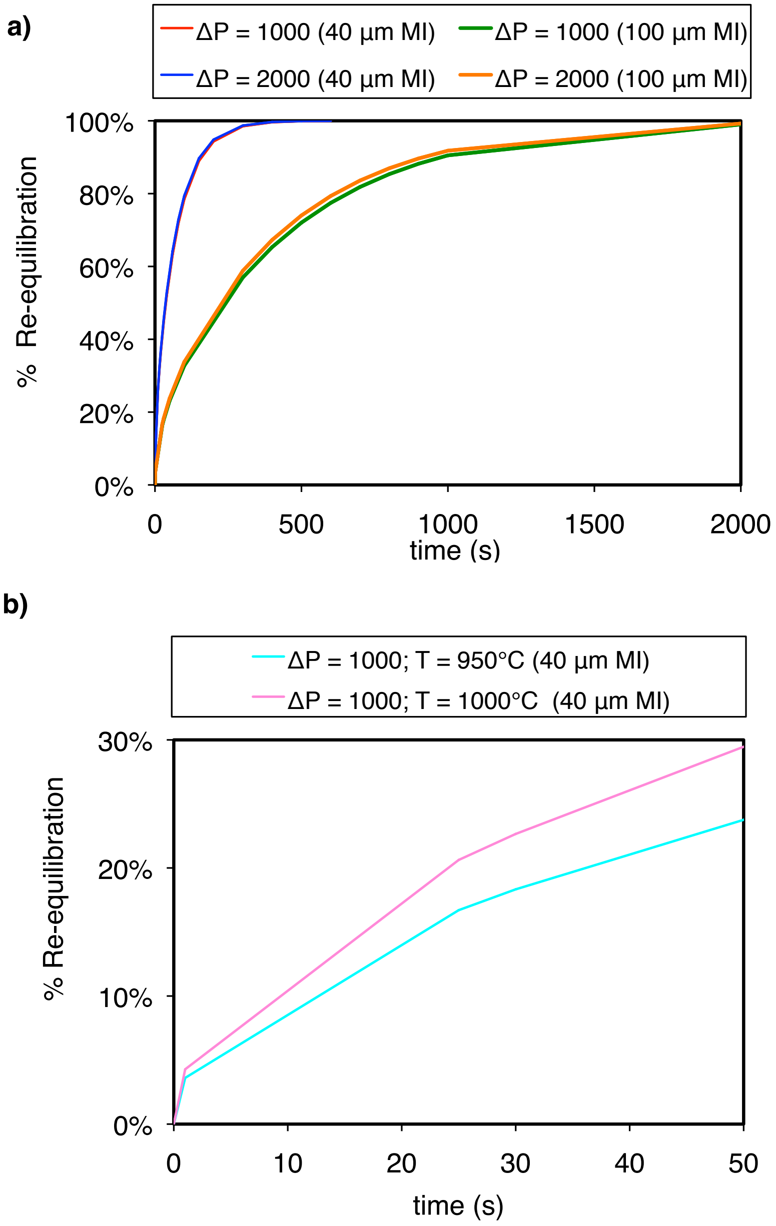

Fig. 6. (a) The percent re-equilibration of CO_2 between melt and vapor bubble for a 40 μm diameter and 100 μm diameter melt inclusion, as calculated with our MATLAB model for the diffusion of CO_2 and H_2O into a vapor bubble. In (a), we assume a constant temperature of 1150°C and an instantaneous pressure drop from 3000 bars to 2000 bars (ΔP = 1000 bars) and 3000 bars to 1000 bars (ΔP = 2000 bars). (b) The percent re-equilibration of CO_2 between melt and vapor bubble during eruption at temperatures of 1000°C and 950°C. This shows that, during the fast timescales (10s of seconds) of post-eruptive cooling, CO_2 diffusion into the bubble significantly slows down. As temperature quickly approaches the glass transition temperature, a negligible amount of CO_2 likely diffuses into the bubble.

temperatures of 950°C and 1000 °C to investigate how much diffusion slows and whether appreciable CO_2 is lost from melt to bubble during eruption. The results suggest that if eruptive cooling and quenching occur on timescales of ~10 seconds (e.g., see Anderson and Brown, 1993, discussion of cooling of tephra in fire fountains), only limited re-equilibration of melt and vapor will occur. As temperatures rapidly decrease from 950-1000°C to the glass transition temperature (~450°C), diffusion of CO_2 into the bubble will virtually cease. This means that during eruptive cooling and quenching, probably a negligible amount of CO_2 is lost to the vapor bubble.

Comparison of Raman and Bubble Formation Model Results

A comparison of the two independent methods that we used to estimate the original CO_2 concentrations of melt inclusions at the time of trapping is shown in Figure 7. For the purpose of comparison, we refer to the two methods as Raman-restored and model-restored. Many melt inclusions show reasonably good agreement between the two methods (for 9 of 17 inclusions, the two methods are within ±500 ppm CO_2), but with a slight offset such that the model values are higher than the Raman-restored values. Most melt inclusions that had carbonate in the bubble or no detectable CO_2 during Raman analysis of the bubble show higher model-restored values than Raman-restored values, as expected. For such inclusions, Raman-restored values can underestimate the amount of CO_2 in the bubble because we cannot quantify the amount of CO_2 in carbonate crystals, and vapor bubbles for which we could not detect CO_2 may actually have CO_2 that was not detected during analysis because the laser was not focused appropriately on the vapor bubble.

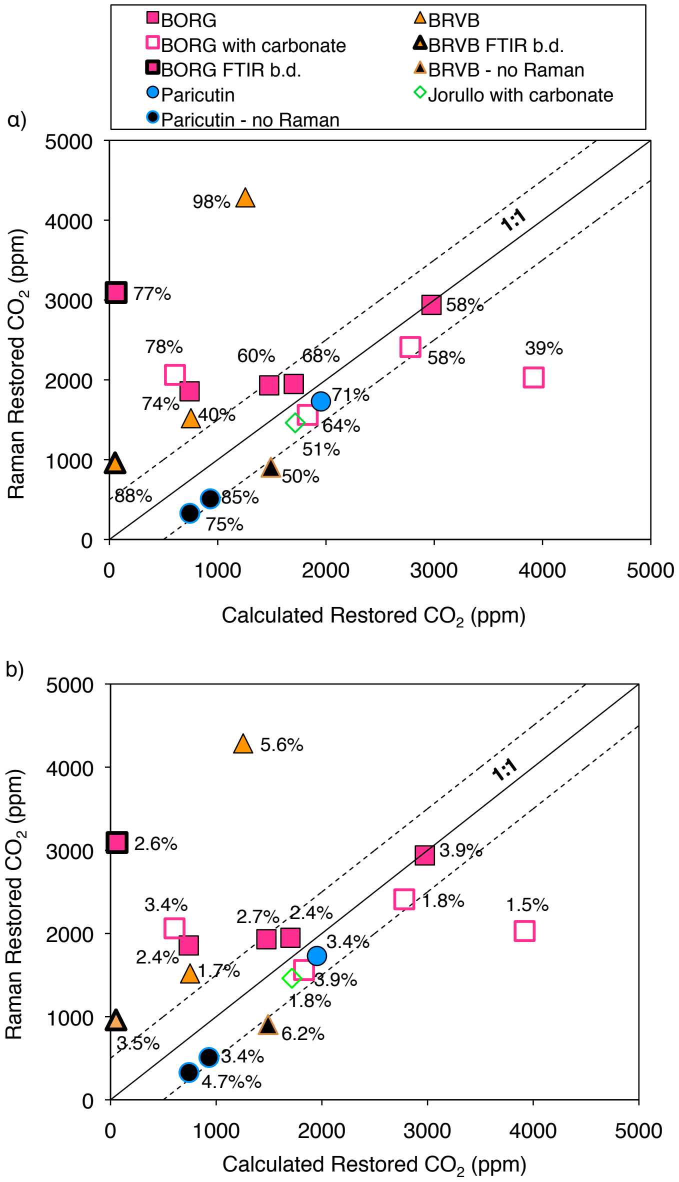

Fig. 7. Comparison of melt inclusion CO_2 values restored by the model method (x-axis) and melt inclusion CO_2 values restored by measuring CO_2 density in the bubble with the Raman spectrometer and then adding that CO_2 back into the glass (y-axis). Black line shows 1:1 relationship, and dashed lines represent ±500 ppm CO_2. Bubbles that have undergone large extents of H_2O loss, such as those from BRVB and some from BORG, have larger Raman-restored values than model-restored values. This is shown in (a), where data labels indicate the percentage of H_2O loss for each inclusion. Furthermore, (b) shows that all melt inclusion volumes are below the maximum bubble volumes calculated for each volcano.

A subset of the melt inclusions has distinctly higher Raman-restored values than model-restored values. All of these melt inclusions have anomalously low H_2O compared to other inclusions from the samples (Fig. 7a). This suggests that these inclusions may have been affected by post-entrapment diffusive H^+ loss, which causes the modeling procedure to underestimate the original CO_2 because loss of H^+ causes the pre-eruption bubble to be larger than it would be due to crystallization and cooling alone (e.g., Bucholz et al., 2013). The alternative possibility that these melt inclusions are inclusions in which melt plus a vapor bubble were co-entrapped is not supported by the comparison of the bubble sizes with the maximum calculated pre-eruption bubble (see Figs. 3, 7b).

Hydrogen Loss and H_2O Reconstructions

It has been shown experimentally that diffusive H^+ (proton) loss from melt inclusions can occur on timescales as short as an hour (Gaetani et al., 2012; Lloyd et al., 2012; Bucholz et al., 2013). To explore the extent to which diffusive H^+ loss from melt inclusions in our study might have contributed to vapor bubble formation, we estimated the magnitude of potential H_2O loss. To do this, we assumed that the highest H_2O/K_2O values from melt inclusions in each volcano were representative of melt inclusions before any diffusive H^+ loss. Then for each melt inclusion we were able to estimate the H_2O concentration before any diffusive loss and compare it to the actual measured value. This method should give us an upper limit for diffusive loss from each melt inclusion, because it is possible that a melt inclusion was trapped from already partially degassed melt (e.g., see Lloyd et al., 2012), whereas we assume that they were all trapped from undegassed melts. For melt inclusions for which we had no electron microprobe data but had FTIR data, we used an average K_2O concentration from each volcano to estimate the original H_2O concentration.

The estimated extent of diffusive H_2O loss for each melt inclusion is compared to measured bubble volume percent in Figure 8. Although there is considerable scatter in the data, the results suggest that H^+ loss is linked to the growth of large bubbles in melt inclusions from these sample suites. This can also be observed in Figure 5a, where large percentages of H_2O loss correspond to higher Raman-restored melt inclusion CO_2 values.

Melt Inclusion Trapping Pressures

We used the reconstructed H_2O and CO_2 concentrations to estimate the original trapping pressures of the melt inclusions and to examine the extent to which post-entrapment bubble formation and diffusive H^+ loss result in lower apparent pressures. Vapor saturation pressures (Fig. 9) were calculated using the solubility relations of Iacono-Marziano et al. (2012) and Papale et al. (2006). Using the analyzed H_2O and CO_2 values of the melt inclusions, vapor saturation pressures range from 161–2054 bars for BORG, 61–1238 bars for BRVB, 758–1645 bars for Paricutin, and 1058–1313 bars for Jorullo. With Raman-corrected CO_2, the pressures are significantly higher, from 1544–3570 bars for BORG, 905–5473 bars for BRVB, 768–2184 bars for Paricutin, and 1140–5414 bars for Jorullo. After correcting for both CO_2 loss and H^+ loss, the reconstructed pressures range from 2358–3915 bars for BORG, 1475–5167 bars for BRVB, 3131–4226 bars for Paricutin, and 2467–5454 bars for Jorullo. These H_2O corrections are the maximum possible original H_2O values. Our results show that the decrease in melt inclusion CO_2 concentration that is caused by post-entrapment bubble formation has a significant effect on inferred pressure of trapping. Loss of H^+ by diffusion also affects the inferred trapping pressure, but to a lesser extent than CO_2 does.

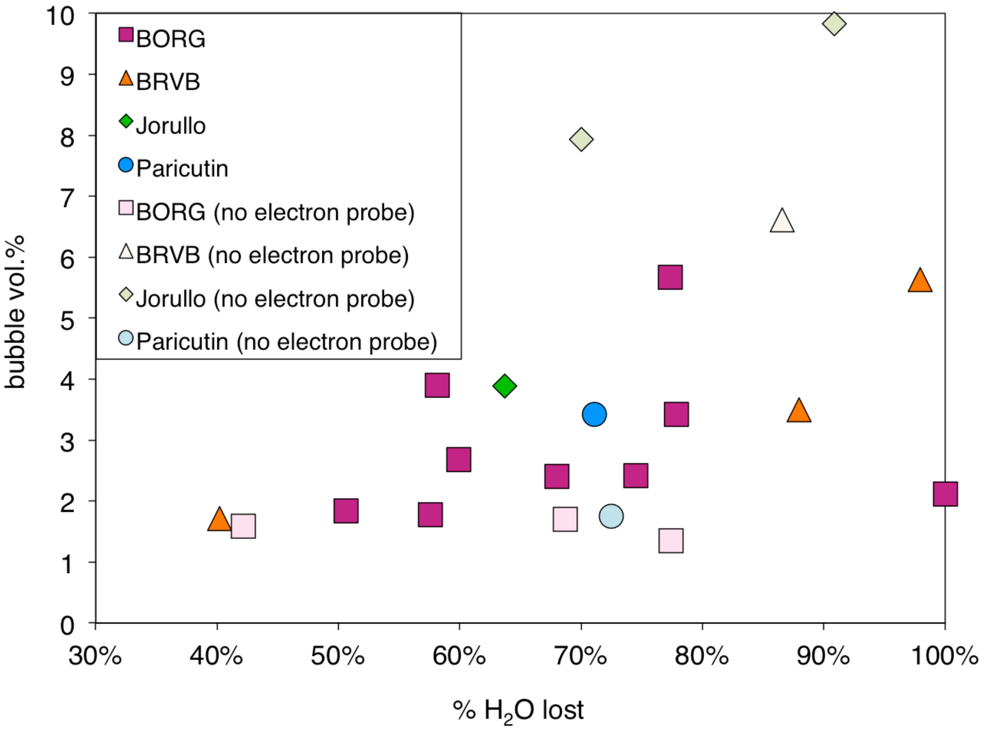

Fig. 8. The amount of initial dissolved H_2O that may have been lost by post-entrapment diffusive H^+ loss (% H_2O lost) versus the size of the bubble as a percentage of the total melt inclusion volume, or bubble volume %. A positive correlation between bubble volume percent and calculated percent H_2O lost suggests that large bubbles (especially those from BRVB and Jorullo samples) formed as a result of diffusive H^+ loss.

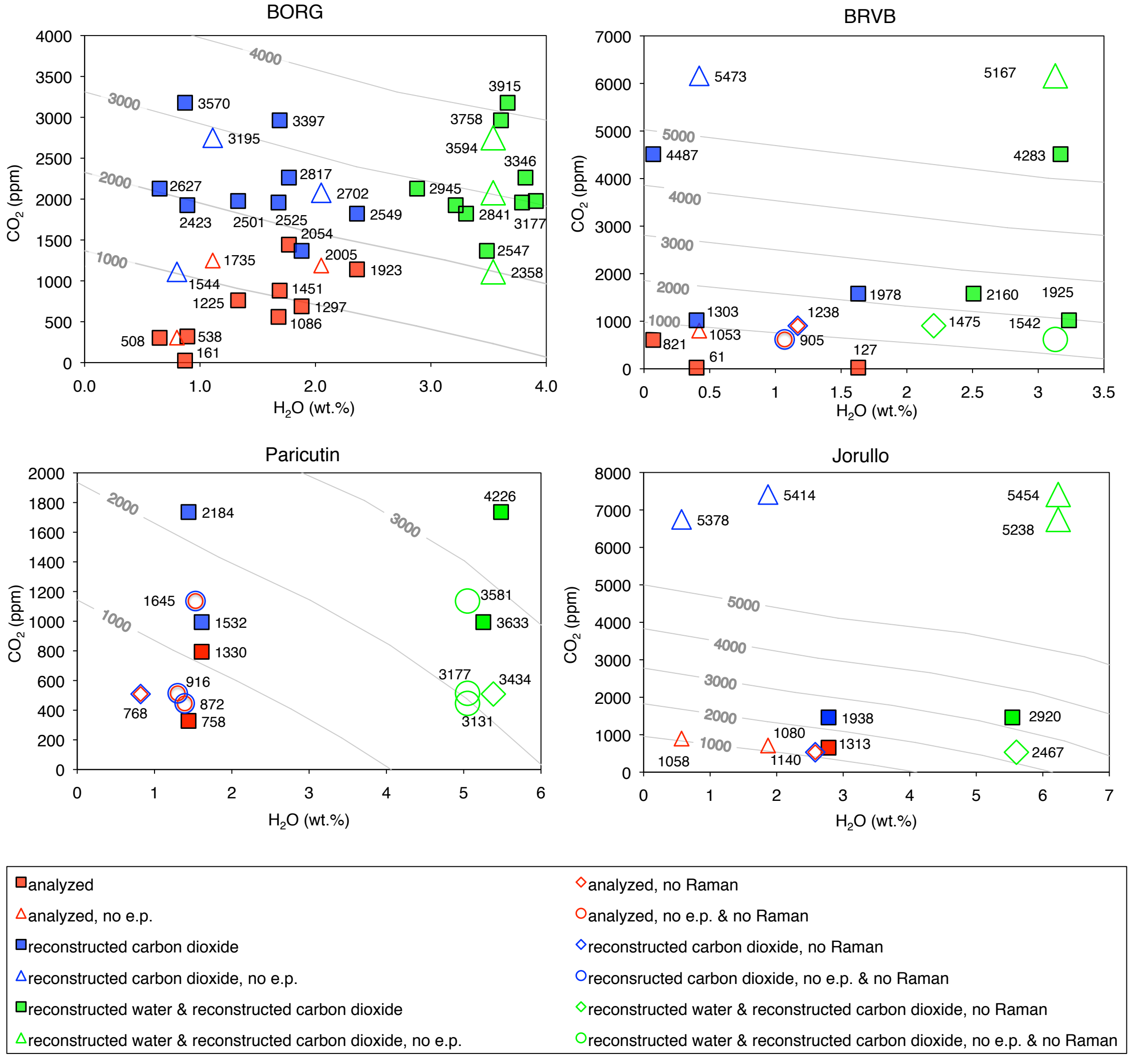

Fig. 9. Pressure reconstructions using analyzed CO_2 and H_2O concentrations (red), corrected CO_2 and analyzed H_2O concentrations (blue), and corrected CO_2 concentrations and corrected (for diffusive H^+ loss) H_2O concentrations (green). Grey lines are isobars calculated using the model of Papale et al. (2006). Data labels next to points are pressures calculated using Iacono-Marziano et al. (2012). Open symbols show melt inclusions for which vapor bubble CO_2 was below detection (diamonds), no electron microprobe data was gathered from the glass (triangles), and for which there was both no electron microprobe data and no CO_2 measured in the bubble (circles). The results show that analyzed values can drastically underestimate pressures if concentrations are not corrected for CO_2 loss or H_2O loss.

CHAPTER V

CONCLUSION

The results of this study lead to a growing body of evidence that post-entrapment bubble formation in melt inclusions can dramatically decrease the concentration of dissolved CO_2 in the included melt. Our conclusion reiterates the importance of post-entrapment melt inclusion modification due to CO_2 diffusion into vapor bubbles and H^+ diffusion (effectively, H_2O loss) out of melt inclusions. As a result, estimates of melt inclusion entrapment pressures based on dissolved H_2O and CO_2 concentrations will typically underestimate the true pressure of trapping, unless the melt inclusions are bubble free.

Our calculations of vapor bubble volumes as result of ΔT (the difference between eruptive and trapping temperatures) tailored for each volcano's composition show that during cooling and post-entrapment crystallization, melt density decreases so that pre-eruptive bubble growth is solely the result of post-entrapment crystallization. During eruption, however, the melt in the inclusion thermally contracts more than the olivine host, causing pre-eruptive bubbles to expand greatly. We demonstrate with a model of H_2O and CO_2 diffusion that the timescales for this eruptive phase likely result in a negligible contribution of CO_2 to the vapor bubble, especially for larger inclusions.

We also show that the original concentration of dissolved CO_2 at the time of trapping can be established using Raman-measured, vapor bubble CO_2 densities as well as by mass balance methods using calculated pre-eruptive bubble volumes. However, CO_2 reconstructions using these two methods can be complicated by the growth of carbonate crystals on the melt inclusion-bubble interface (effectively removing CO_2 from the vapor bubble and therefore decreasing CO_2 densities measured by Raman spectroscopy) and the diffusive loss of H^+ out of the melt inclusion (which increases the bubble volume fraction). Thus, it is advisable that both reconstruction methods be employed for comparison when reconstructing melt inclusion CO_2 concentrations. Furthermore, inclusions with low H_2O concentrations compared to H_2O concentrations from other samples are suspect as they might have low H_2O concentrations due to H^+ loss.

APPENDIX A

BUBBLE VOLUME CALCULATIONS

After a clear photograph of each melt inclusion and hosted bubble was taken using the camera on the Raman spectrometer, a micrometer scale was placed under the microscope ocular to calibrate the sizes of objects in the photos. This was done for the 10x, 40x, and 100x objectives. Using this calibration, the vertical and horizontal diameters of each bubble were determined. Most bubbles are nearly circular, but we measured both the vertical and horizontal axes so an average diameter could be used for the bubble volume calculation. Bubbles volumes were then calculated using the volume of a sphere

$$V_{bubble} = \frac{4}{3} \times \pi \times \left(\frac{r_{bubble}^{h} + r_{bubble}^{v}}{2} \right)^{3}$$

where V_{bubble} is the volume of the bubble (μm^3), r_{bubble}^{h} is the horizontal radius of the bubble (μm), and r_{bubble}^{v} is the vertical radius of the bubble.

Because time using the Raman spectrometer at Virginia Tech was limited, all the vertical and horizontal diameters for every bubble were measured using the Raman camera and then pictures of each melt inclusion and hosted bubble were brought back to the University of Oregon to measure melt inclusion parameters using ImageJ, a program that counts pixels in a photograph to measure distances. We measured the vertical and horizontal axes of each bubble using ImageJ and, because we knew the actual length of each bubble's vertical and horizontal axis, we calculated a conversion multiplier to allow us to convert unitless transects measured in ImageJ to actual lengths in micrometers. We used the relationship

$$M = d_{bubble}/d_{ImageJ}$$

where M is the conversion multiplier between ImageJ transects and actual lengths in micrometers, d_{bubble} is the actual diameter of the bubble (µm) determined using the Raman spectrometer camera and carefully calibrated distances (detailed above), and d_{ImageJ} is the diameter of the bubble measured in ImageJ. We calculated M using both the vertical and horizontal axis of each bubble; although the conversion multiplier was nearly similar for each axis, we calculated melt inclusion volume using both axes to estimate error.

Then, using ImageJ, we measured the longest axis and the shortest axis (perpendicular to the longest axis) of each melt inclusion. We assumed that the third, unobservable ellipsoidal axis was equal to the smallest measured axis on each melt inclusion. We then used the conversion multipliers obtained from each bubble axis measurement (one from the vertical axis of the bubble, and one from the horizontal axis of the bubble) to calculate two ellipsoidal volumes (V_{MI}) for each melt inclusion:

$$V_{MI} = \frac{4}{3} \times \pi \times r_{MI}^{l} \times (r_{MI}^{s})^2$$

where r_{MI}^{l} is the radius of the long axis of the melt inclusion and r_{MI}^{s} is the radius of the short axis of the melt inclusion.

Next, we used the spherical bubble volume (V_{bubble}) and the two melt inclusion ellipsoidal volumes (V_{MI}) to determine the volume percent ($vol.\%$) of the melt inclusion that is a vapor bubble:

$$vol.\% = 100 \times \frac{V_{bubble}}{V_{MI}}$$

Because we calculated two melt inclusion volumes using the two different conversion multipliers, we were also able to estimate error using the standard deviation of calculated bubble volumes.

APPENDIX B

FTIR THICKNESS MEASUREMENTS AND OLIVINE INTERFERENCE CORRECTIONS

The thickness of the melt inclusion is a parameter used in calculating the concentrations of H_2O and CO_2 with Beer's Law, so it is important to accurately determine the thickness. Before removing the olivine wafers from epoxy for FTIR analysis, we measured sample wafer thickness. To do this, we used a micrometer to make multiple measurements of the thickness of the glass slide. We then measured the thickness of the glass slide + olivine wafer. The average thickness of the glass slide was then subtracted from the thickness of the glass slide + olivine wafer to determine the thickness of just the olivine wafer.

Next, these wafer thicknesses were compared to wafer thicknesses calculated using interference fringes from two reflectance spectra for the host crystal for each inclusion. The spacing of the fringes in reflectance spectra has a relationship with melt inclusion thickness (Wysoczanski and Tani, 2006; Fig. B1). The mathematical relationship between cycles and wavenumbers is expressed as

$$T = \frac{m}{2n \times (V_1 - V_2)}$$

where m is the number of waves in the selected wavenumber range, n is the refractive index of the mineral (for olivine, 1.66), and V_1 and V_2 are the highest and lowest wavenumbers, respectively. For most melt inclusions the micrometer thickness measurement was slightly larger than the average thickness calculated using the reflectance spectra (Fig. B2). As such, reflectance spectra were used for all thickness values except in the cases where reflectance spectra did not show clear interference

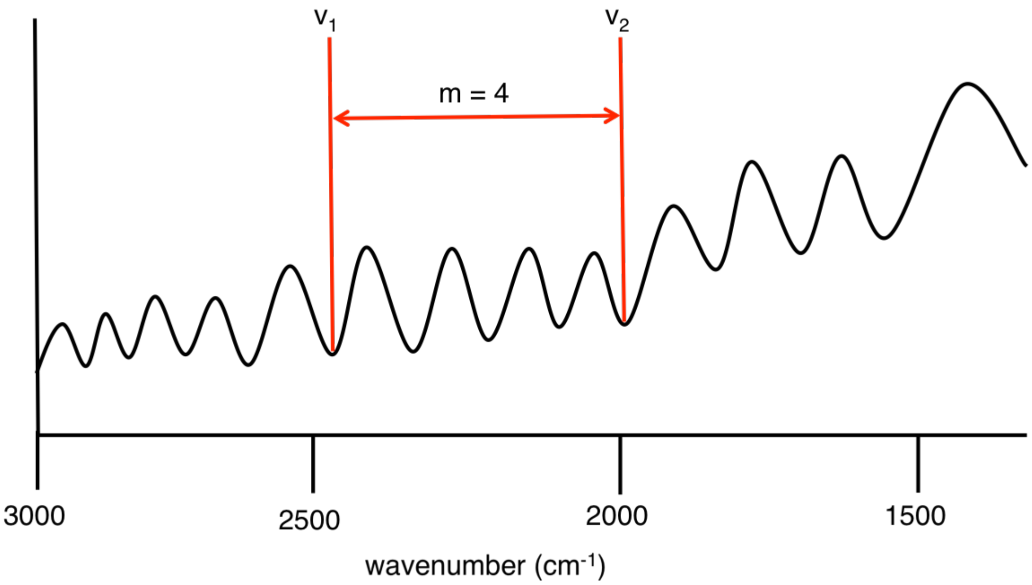

Fig. B1. Sketch of reflectance fringes from a FTIR spectrum, where the x-axis is the wavenumber and the y-axis is absorbance. The number of troughs or peaks between a given range of wavenumbers has a relationship with wafer thickness. Finding the most symmetrical portion of the undulating curve of a reflectance spectrum is key for accurate wafer thickness calculations. In this example spectrum, the number of waves is 4, and v_1 and v_2 show the high and low wavenumbers, respectively.

fringes or for melt inclusions with reflectance-calculated thicknesses >10 µm larger than micrometer thicknesses.

Some melt inclusions were too small (<30 µm) to be intersected on both sides of the olivine wafer during polishing. For these inclusions, olivine Si-O peaks can be seen in absorption spectra between approximately 2000 and 1700 cm^{-1}. Often, a prominent peak can be seen around 1770 cm^{-1}. To correct the thickness measurements for the presence of olivine, we first measured the absorbance of the olivine peak at 1770 cm^{-1} in the melt inclusion absorption spectrum and then measured the absorbance of the olivine peak at 1770 cm^{-1} in an absorption spectrum taken on the olivine wafer. The thickness of the melt

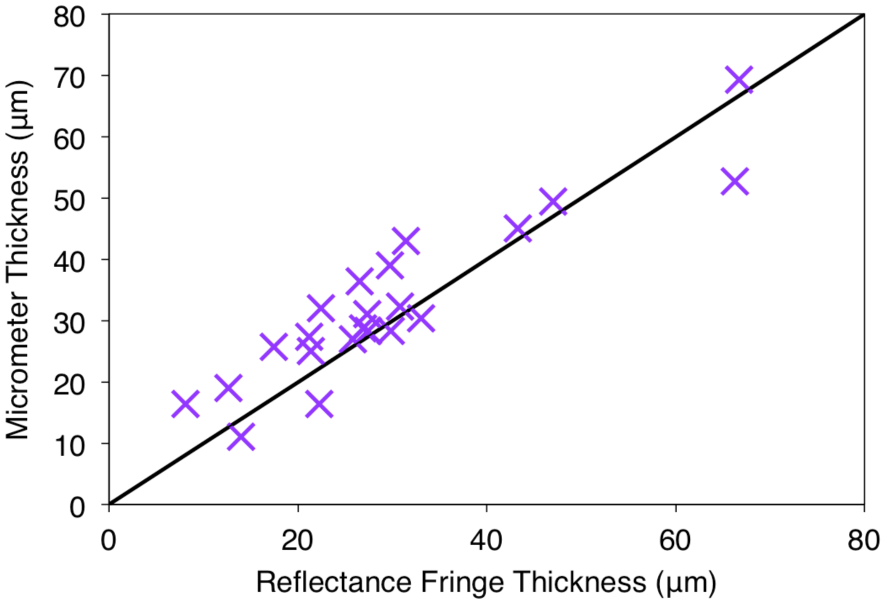

Fig. B2. Comparison of thickness determined using a micrometer and the average thickness calculated using two interference fringes for each melt inclusion. Most micrometer thicknesses overestimate the thickness of the wafer, so interference fringe thicknesses were used for most melt inclusions.

inclusion to be used in the Beer's Law calculation could then be calculated using a ratio of these olivine peak heights using the relationship

$$T_{corrected} = T_{original} \times \left(1 - \frac{A_{MI}^{1770}}{A_{olivine}^{1770}}\right)$$

where $T_{corrected}$ is the corrected thickness of the melt inclusion, $T_{original}$ is the measured thickness of the overall wafer (either calculated using reflectance spectra or measured with the micrometer), A_{MI}^{1770} is the absorbance of the olivine peak at 1770 cm^{-1} in the melt inclusion absorption spectrum, and $A_{olivine}^{1770}$ is the absorbance of the olivine peak at 1770 cm^{-1} in the olivine absorption spectrum (Nichols and Wysoczanski, 2007).

APPENDIX C

DETAILED MAXIMUM BUBBLE PERCENT CALCULATIONS

Assuming no diffusive H^+ loss, post-entrapment vapor bubble growth in a melt inclusion is the result of post-entrapment crystallization and thermal contraction of the melt more than thermal contraction of the host. To explore vapor bubble growth for each volcano, we calculated the relationship between the maximum bubble volume percent and the difference between eruptive and formation temperatures (ΔT). This was done in three steps. Fist, we calculated the volume of bubble formed as a result of post-entrapment crystallization. Then, we calculated the volume of bubble formed as a result of thermal contraction of the melt in the melt inclusion down to the glass transition temperature. Last, we modified bubble volumes calculated in Step 1 and Step 2 by the thermal contraction of the olivine host. These calculations allowed us to screen out bubbles that were co-entrapped with the melt when the inclusion formed rather than being post-entrapment in origin. In addition, these calculations illuminated the relative roles of post-entrapment crystallization and thermal contraction in forming vapor bubbles.

Step 1: Vapor Bubble Growth as a Result of Post-entrapment Crystallization

We first calculated the effect of post-entrapment crystallization on decreasing the volume inside a melt inclusion, assuming that any volume deficit formed as a result of cooling and crystallization was equal to the size of the vapor bubble formed. Using rhyolite-MELTS (Gualda et al., 2012), we crystallized (at constant pressure) the most primitive (low SiO_2 and high MgO) melt composition from each volcano. To determine H_2O concentration for each primitive melt, we took the highest H_2O/K_2O ratio and multiplied it by the K_2O composition of the primitive composition. Also, we paired each primitive composition with the highest CO_2 concentration. We used these CO_2 and H_2O concentrations to calculate the pressure of crystallization in VolatileCalc. The pressures for crystallization were 2.88 kbars for BORG, 1.76 kbars for BRVB, 3.80 kbars for Jorullo, and 4.02 kbars for Paricutin.

For each crystallization sequence, we started crystallization at the liquidus temperature (determined by rhyolite-MELTS) and ended crystallization at 140°C below the liquidus temperature. We crystallized melt in temperature steps of 20°C. For each temperature step, rhyolite-MELTS recorded a liquid mass (g), liquid density (g/cm^3), olivine mass (g), olivine density (g/cm^3), and the concentrations of major elements and H_2O in the melt. In addition, we calculated melt densities at each temperature using the melt composition, temperature, and coefficients from Lange and Carmichael (1990).

Using the liquid (melt) mass and melt density, we calculated the melt volume (V_{melt}^{PEC}) at each temperature step. Additionally, using the olivine mass and the olivine density, we calculated the volume of olivine ($V_{olivine}^{PEC}$) formed at each temperature step. Although slight over the 140° of cooling and crystallization, host olivine also contracts. To reflect the host olivine thermal contraction, we amended the cavity volume by the amount the olivine host contracts for each 20° temperature step. For more information on calculating the contraction of olivine, see Step 3, below. The fraction bubble volume formed (ϕ_{bubble}^{PEC}) as a result of post-entrapment crystallization and olivine contraction at each temperature step can then be calculated using:

$$\phi_{bubble}^{PEC} = \frac{\left(V_{cavity}^{PEC} - \left[V_{melt}^{PEC} + V_{olivine}^{PEC}\right]\right)}{V_{cavity}^{PEC}}$$

where V_{cavity}^{PEC} is the volume of the cavity. This allows us to estimate a maximum, pre-eruptive bubble volume for each volcano. We noted that, over the 140° of cooling, the melt density decreases due to an increase in H_2O and decrease in FeO and MgO. As such, bubbles formed during this step are the result of only olivine crystallization, and not contraction of the melt.

Step 2: Melt Thermal Contraction to the Glass Transition Temperature

Next, assuming no olivine crystallization, we calculated the volume change of melt in a melt inclusion as a result of the melt thermally contracting down to the glass transition temperature. To calculate the extent of melt thermal contraction, we first had to determine glass transition temperatures. This is important because the glass transition temperature is the temperature at which we assume a cooling melt will stop contracting. To do this, we used a logarithmic regression of glass transition temperatures in basaltic melts (Giordano et al., 2005) to determine the approximate relationship between H_2O content (wt.%) and the temperature (°C) of the onset of the glass transition (T_{GT}^{onset}) (Fig. C1). We then used this mathematical relationship to determine glass transition temperatures for melts of varying initial H_2O content.

Next, we used the rhyolite-MELTS melt composition at each 20° temperature step and coefficients from Lange and Carmichael (1990) to calculate the density of the melt. With this information, we could calculate the liquid volume ($V_{melt}^{Th.C.MI}$) associated with each temperature step as a result of thermal contraction:

$$V_{melt}^{Th.C.MI} = \frac{1}{\rho_{melt}^{Th.C.}} \times m$$

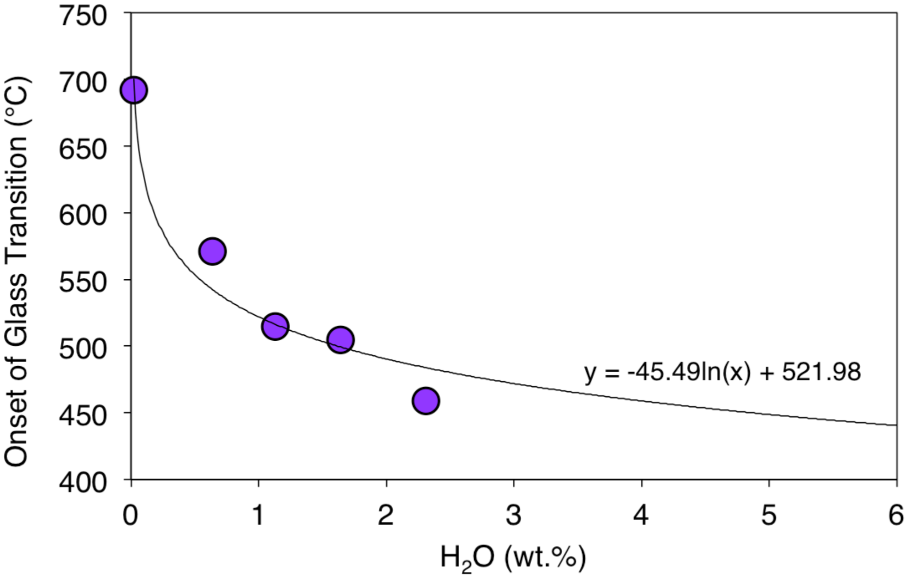

Fig. C1. Relationship between melt H_2O concentration and the onset of the glass transition. Symbols represent experimental data points from Giordano et al. (2005). The logarithmic regression line shows the best-fit relationship between H_2O and the glass transition temperature.

where $\rho_{melt}^{Th.C.}$ is the density of the liquid at each temperature step, and m is the liquid mass, which we assumed was 100 g. Then, using the same melt composition at each temperature step, we calculated the density of the melt at the glass transition temperature. Assuming that we still had 100 grams of melt at the glass transition temperature, we could calculate a volume of melt at the glass transition temperature. Thus, the volume change ($\Delta V_{melt}^{Th.C.}$) is

$$\Delta V_{melt}^{Th.C.} = V_{melt}^{Th.C.} - V_{melt}^{GT}$$

where V_{melt}^{GT} is the volume of melt at the glass transition temperature for each temperature step and $V_{melt}^{Th.C.}$ is the volume of the melt at high temperature, at the beginning of the eruptive cooling stage. The void space formed as a result of the contraction of the melt phase, or the volume fraction void space ($\phi_{melt}^{Th.C.MI}$) as a result of melt contraction, is caculated by

$$\phi_{melt}^{Th.C.MI} = \frac{\Delta V_{melt}^{Th.C.}}{V_{melt}^{Th.C.}}$$

where $\Delta V_{melt}^{Th.C.}$ is the change in volume of the melt as a result of thermal contraction at each temperature step and $V_{melt}^{Th.C.}$ is the volume of the melt as a result of thermal contraction at each temperature step.

Step 3: Host Olivine Contraction

Finally, we calculated the the extent of thermal contraction of the olivine host to the glass transition temperature. We used a value of 43.95 cm^3/mol (Kumazawa and Anderson, 1968) for the volume of olivine at ambient temperature ($V_{olivine}^{ambient}$). The isobaric change in volume for a change in temperature, $\left(\frac{\delta V}{\delta T}\right)_P$ is expressed by

$$\left(\frac{\delta V}{\delta T}\right)_P = \alpha \times V_{olivine}^{ambient}$$

where α is the thermal expansion coefficient and $V_{olivine}^{ambient}$ is the volume of olivine at ambient temperature. This relationship can be used to calculate the extent of host olivine contraction as a result of cooling.

For example, to modify the cavity volume during Step 2, we wanted $\left(\frac{\delta V}{\delta T}\right)_P$ to be expressed over the range of temperatures between the glass transition temperature and eruptive temperature. So, we used an average α value from experimental data of olivine expansion (Suzuki, 1975) over the range of these temperatures. The volume change between olivine at the eruptive temperature and olivine at ambient temperature ($\Delta V_{olivine}^{eruptive}$) can be calculated by

$$\Delta V_{olivine}^{eruptive} = \left(\frac{\delta V}{\delta T}\right)_P \times \Delta T_{eruptive-ambient}$$

where $\Delta T_{eruptive-ambient}$ is the difference between the eruptive and ambient temperatures. The volume of olivine at the temperature of eruption ($V_{olivine}^{eruptive}$) is therefore

$$V_{olivine}^{eruptive} = V_{olivine}^{ambient} + \Delta V_{olivine}^{eruptive}$$

where $V_{olivine}^{ambient}$ is the volume of olivine at an ambient temperature and $\Delta V_{olivine}^{eruptive}$ is the volume change between erupted olivine and ambient olivine calculated above. Similarly, the change in volume between olivine at the glass transition temperature and at ambient temperature ($\Delta V_{olivine}^{GT}$) can be calculated by

$$\Delta V_{olivine}^{GT} = \left(\frac{\delta V}{\delta T}\right)_P \times \Delta T_{GT-ambient}$$

where $\Delta T_{GT-ambient}$ is the difference between the glass transition temperature and the ambient temperature. The volume of olivine at the glass transition temperature, $V_{olivine}^{GT}$, is therefore given by

$$V_{olivine}^{GT} = V_{olivine}^{ambient} + \Delta V_{olivine}^{GT}$$

where $V_{olivine}^{ambient}$ is the volume of olivine at ambient temperature and $\Delta V_{olivine}^{GT}$ is the change in volume between olivine at the glass transition temperature and olivine at ambient temperature, as calculated above.

Finally, we claculated the fractional decrease in the volume of olivine ($f_{olivine}^{Step2}$) a result of thermal contraction between the eruptive and glass transition temperatures:

$$f_{olivine}^{Step2} = \frac{V_{olivine}^{GT}}{V_{olivine}^{eruptive}}$$

where $V_{olivine}^{eruptive}$ is the volume of olivine at eruption and $V_{olivine}^{GT}$ is the volume of olivine at the glass transition temperature. A similar calculation was done for contraction of olivine during Step 1:

$$f_{olivine}^{Step1} = \frac{V_{olivine}^{pre-eruptive}}{V_{olivine}^{trapping}}$$

where $f_{olivine}^{Step1}$ is the fractional decrease in the volume of olivine as a result of thermal contraction between entrapment and pre-eruptive (but post-entrapment) temperatures, $V_{olivine}^{pre-eruptive}$ is the volume of olivine at each pre-eruptive (put post-entrapment) temperature, and $V_{olivine}^{trapping}$ is the volume of olivine at the trapping temperature.

Using these calculations, we modified the cavity volume in Step 1 (V_{cavity}^{Step1}) as a result of thermal contraction of the olivine host:

$$V_{cavity}^{Step1} = V_{cavity}^{trapping} \times f_{olivine}^{Step1}$$

where $V_{cavity}^{trapping}$ is the volume of the cavity at the trapping temperature and $f_{olivine}^{Step1}$ is the fractional decrease in host olivine during Step 1. Similarly, we calculated the cavity volume in Step 2 (V_{cavity}^{Step2}) as a result of thermal contraction of the olivine host from the eruptive temperature to the glass transition temperature:

$$V_{cavity}^{Step2} = V_{cavity}^{pre-eruptive} \times f_{olivine}^{Step2}$$

where $V_{cavity}^{pre-eruptive}$ is the volume of the cavity at each pre-eruptive temperature (or, each temperature step) and $f_{olivine}^{Step2}$ is the fractional decrease of host olivine during Step 2.

Last, we wanted to determine what the final maximum bubble volume fraction was considering post-entrapment crystallization, thermal contraction of the melt, and thermal contraction of the olivine. This was calculated through adding the volume fraction bubble formed as a result of thermal contraction of the melt and thermal contraction of the olivine (Step 2) to the volume fration bubble formed during post-entrapment crystallization and thermal contraction of the olivine (Step 1).

From this we obtained volume percent bubble, which has a relationship with ΔT. Each melt inclusion's ΔT was determined using the temperature outputs from Petrolog3 for uncorrected compositions (which yield eruptive temperatures) and post-entrapment crystallization and Fe loss corrected compositions (which yield entrapment temperatures). Bubbles that had volume percents above the calculated maximum bubble volume percent were not included in final melt inclusion CO_2 reconstructions because they are likely to be bubbles that were co-entrapped with melt when the inclusion formed.

APPENDIX D

MELT INCLUSION VOLUME VERSUS BUBBLE VOLUME

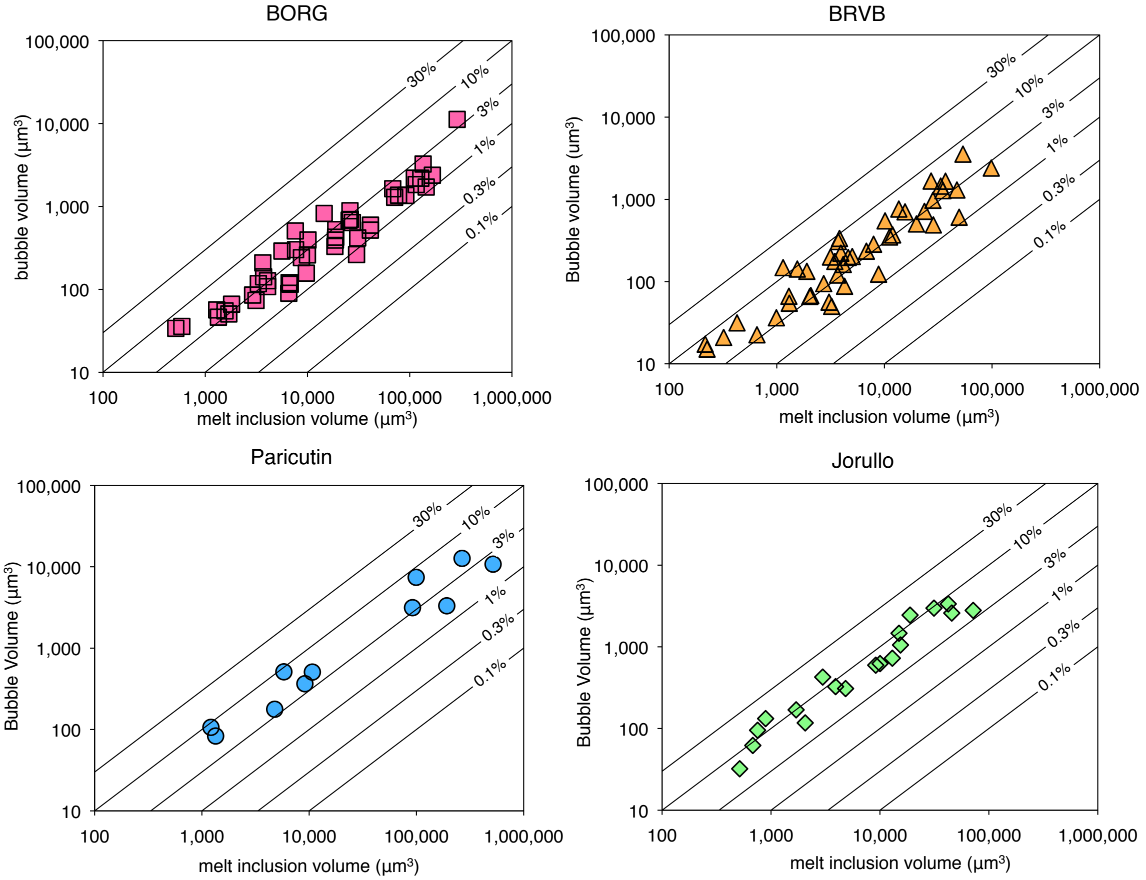

Fig. D1. Melt inclusion volumes plotted against bubble volumes, with lines indicating the percent of the melt inclusion that is occupied by a bubble. Most bubbles are between 1 and 10 vol.%.

APPENDIX F

COMPUTER CODE USED TO CALCULATE TIMESCALES OF CO_2 AND H_2O DIFFUSION IN BASALTIC MELT INCLUSIONS

We developed a MATLAB code to compute the one-dimensional diffusion of CO_2 and H_2O through a melt inclusion (SiO_2 = 49 wt.%) into a vapor bubble. To use the code, the user enters a diffusion duration (s), a starting pressure (3000, 2000, 1000, or 500 bars), an ending pressure (2000, 1000, or 500 bars), a distance from the end of the melt inclusion to the melt inclusion-bubble interface (μm), a vapor bubble radius (μm), an initial H_2O concentration (wt.%), and a density for the basaltic glass (kg/m^3). Assuming vapor saturation, the code utilizes relationships between dissolved H_2O (wt.%), dissolved CO_2 (wt.%), H_2O in the vapor phase (H_2Ov, mol.%), and CO_2 in the vapor phase (CO_2v, mol.%) to calculate the initial CO_2 concentration in the melt inclusion and the initial vapor compositions in the bubble. Relationships between dissolved H_2O, dissolved CO_2, mole fraction H_2O vapor, and mole fraction CO_2 vapor are estimated through linear regression equations from VolatileCalc-generated isobars (Newman and Lowenstern, 2002) and vapor isopleths at 1150°C and pressures of 3000, 2000, 1000, and 500 bars.

After calculating the starting concentrations, the pressure in the melt inclusion instantaneously drops, changing the concentration of H_2O and CO_2 at the first node at the melt inclusion-bubble interface. These new concentrations assume that the mole fractions of H_2Ov and CO_2v do not change during the first time step of the pressure drop: During the first time step, the original mole fractions of H_2O vapor and CO_2 vapor are used to determine the new concentrations of H_2O and CO_2 at the first node after the pressure drop. These new concentrations at the inclusion-bubble interface create a disequilibrium in CO_2 and H_2O concentrations in the melt inclusion, driving diffusion of these volatiles into the vapor bubble.

The code assumes that there is no diffusion of H_2O and CO_2 from the melt inclusion to the host crystal; thus the inclusion-host interface utilizes a no-flux boundary such that the last node equals the previous node's composition. The boundary at the inclusion-bubble interface is more complex; it depends on the mole fractions of CO_2 and H_2O that are in the bubble. For this boundary, at each time step the program calculates the flux of H_2O and CO_2 into the bubble. Using the flux and the surface area of the bubble, the code determines the moles of H_2O and CO_2 that entered the bubble. Using regression equations from VolatileCalc that relate H_2Ov (mol.%) to the concentration of dissolved H_2O (wt.%) in the melt and CO_2v (mol.%) to the concentration of dissolved CO_2 (wt.%) in the melt and assuming equilibrium between the bubble and the first node, the code calculates the new concentration (wt.%) of H_2O and CO_2 at the first node. Both boundaries are updated in each time step.

The code stops running when the user-specified diffusion duration is reached. The code outputs compositions (mol.%) of CO_2 and H_2O in the bubble and diffusion profiles for H_2O and CO_2 in the melt inclusion. A copy of the script with an example of diffusion profiles is shown below.

Contents

- ASSUMPTIONS
- INPUT PARAMETERS
- CONSTANT PARAMETERS
- INITIAL CO2 calc
- Calculate Initial CO2 and H2O in bubble
- INITIALIZE ALL ARRAYS
- Pressure Drop: Node 1 CO2 and H2O concentrations
- Diffusion of H2O and CO2
- Plot Diffusion profiles
- Output Final CO2 and H2O in bubble

```
%1D DIFFUSION OF CO2 AND H2O THROUGH A BASALTIC MELT INCLUSION TO A VAPOR BUBBLE
%Alternatively titled "Double Bubble Trouble"
%Ellen Aster
```

ASSUMPTIONS

```
%No volume change of bubble due to mass influx
%No volume change of melt inclusion due to crystallization or shrinkage
%Melt and bubble are intitally in equilibrium
%Isothermal (T = 1423 K)
%SiO2 = 49 wt.%

clear all
clc
close all
```

INPUT PARAMETERS

```
%Enter diffusion duration (s)
tot_time = 1;

%Enter starting pressure (3000, 2000, or 1000 bars)
P_i = 3000;

%Enter ending pressure (2000, 1000, or 500 bars)
P_f = 1000;

%Enter distance from end of MI to MI-bubble interface (um)
length = 40;

%Enter bubble radius (um)
radius = 10;

%Enter initial H2O concentration (wt. %)
H2O_i = 1.5;
```

```
%Enter density of basalt (kg/m^3) (average of glass densities)
basalt_density = 2669;
```

CONSTANT PARAMETERS

```
T = 1173.15;                       %temperature (K)
nnodes = 25;                    %no. nodes
dx = length/(nnodes-1);         %change of nodes in x-direction (um)
time = 0;                       %time starts at 0
dt = 0.001;                       %time changes by units of 1 second
R = 8.314;                       %gas constant [J/(K * mol)]
H2O_molecular_mass = 18.015;     %molecular mass of H2O (g/mol)
CO2_molecular_mass = 44.01;      %molecular mass of CO2 (g/mol)
```

INITIAL CO2 calc

```
if P_i == 3000
    CO2_i = -30.308 * (H2O_i)^2 -93.138 * H2O_i + 1589.8;
    H2Ov_i = 1.9793 * (H2O_i)^2 + 5.5422 * H2O_i;
    CO2v_i = 0.0644 * (CO2_i) - 0.9135;
    elseif P_i == 2000
        CO2_i = -35.182 * (H2O_i)^2 - 54.217 * H2O_i + 1004.8;
        H2Ov_i = 3.5828 * (H2O_i)^2  + 5.1277 * H2O_i;
        CO2v_i = 0.1013 * CO2_i - 0.7389;
    elseif P_i == 1000
        CO2_i = -42.406 * (H2O_i)^2 - 15.737 * H2O_i + 476.54;
        H2Ov_i = 19.95 * (H2O_i)^2 + 0.8391 * H2O_i;
        CO2v_i = 0.4309 * CO2_i - 0.3914;
end

%Outputs initial CO2 (ppm)
CO2_i;

%Outputs initial H2O in vapor phase (mol.%)
H2Ov_i;

%Outputs initial CO2 in vapor phase (mol.%)
CO2v_i;
```

Calculate Initial CO2 and H2O in bubble

```
%radius (m)
radius_meters = radius/(10^6);

%volume of bubble (m^3)
bubble_volume = 4/3 * pi * radius_meters^3;

%initial pressure (Pa)
P_i_Pa = P_i * 100000;

%Solve for moles H2O and CO2 using Ideal Gas Law
```

```
moles_total_i = (P_i_Pa * bubble_volume)/(R * T);
moles_H2O_i = moles_total_i * (H2Ov_i/100);
moles_CO2_i = moles_total_i * CO2v_i/100;
```

INITIALIZE ALL ARRAYS

```
%CO2, H2O, dD_CO2, dD_H2O, d_H2O, d_CO2, d2_H2O, d2_CO2, D_H2O, D_CO2 Length Arrays

%CO2 and H2O concentration arrays
CO2_array = zeros(nnodes, 1);
H2O_array = zeros(nnodes, 1);


%initial concentrations in H2O and CO2 arrays
for k = 1:nnodes
    CO2_array(k) = CO2_i;
    H2O_array(k) = H2O_i;
end

%first derivative of diffusivity arrays
dD_CO2 = zeros(nnodes, 1);
dD_H2O = zeros(nnodes, 1);

%first derivative of concentration arrays
d_H2O_array = zeros(nnodes, 1);
d_CO2_array = zeros(nnodes, 1);

%second derivative of concentration arrays
d2_H2O_array = zeros(nnodes, 1);
d2_CO2_array = zeros(nnodes, 1);

%diffusivity array
D_H2O = zeros(nnodes,1);
D_CO2 = zeros(nnodes,1);

%set up length array (i.e. x-axis)
length_array = zeros(nnodes,1);
length_array(1) = 0;
for i = 2:nnodes
    length_array(i) = length_array(i - 1) + dx;
end
```

Pressure Drop: Node 1 CO2 and H2O concentrations

```
% calculate concentration at node 1 after pressure drop
if P_f == 2000
        H2O_node = 3.85 * 10^-9 * H2Ov_i^5 - 1.10 * 10^-6 * H2Ov_i^4 + 1.18 * 10^-4 * H2Ov_i^3
 - 5.93 * 10^-3 * H2Ov_i^2 + 1.75 * 10^-1 * H2Ov_i;
        CO2_node = 9.8667 * CO2v_i + 7.4644;
    elseif P_f == 1000
        H2O_node = 2.97 * 10^-9 * H2Ov_i^5 - 8.51 * 10^-7 * H2Ov_i^4 + 9.14 * 10^-5 * H2Ov_i^3
 - 4.59 * 10^-3 * H2Ov_i^2 + 1.32 * 10^-1 * H2Ov_i;
        CO2_node = 4.7266 * CO2v_i + 2.5497;
    elseif P_f == 500
```

```
        H2O_node = 2.11 * 10^-9 * H2Ov_i^5 - 6.08 * 10^-7 * H2Ov_i^4 + 6.57 * 10^-5 * H2Ov_i^3
 - 3.34 * 10^-3 * H2Ov_i^2 + 9.65 * 10^-2 * H2Ov_i;
        CO2_node = 2.3201 * CO2v_i + 0.9244;
end

% update node 1 with concentration after pressure drop
CO2_array(1) = CO2_node;
H2O_array(1) = H2O_node;
```

Diffusion of H2O and CO2

```
%Update H2O_moles_bubble to be value of moles_H2O_i
H2O_moles_bubble = moles_H2O_i;
CO2_moles_bubble = moles_CO2_i;

while time < tot_time

    %Calculate H2O and CO2 Diffusivity constants
    for i = 1:nnodes
        %Update H2O diffusivity constant
        D_H2O(i) = H2O_array(i) * exp(-8.56 - 19110/T) * (0.057 * log(length) + 0.0732) * 10^1
2;
        %Update CO2 diffusivity constant
        D_CO2(i) = exp(-13.99 - (17367 + (1944.8 * (P_f * 0.0001)))/T + (855.2 + (271.2 * (P_f
 * 0.0001)))/T * H2O_array(i))*10^12;
    end

    %update all the derivatives
    for i = 2:nnodes - 1;
        dD_CO2(i) = (D_CO2(i+1) - D_CO2(i -1))/(2*dx);
        dD_H2O(i) = (D_H2O(i+1) - D_H2O(i -1))/(2*dx);
        d_H2O_array(i) = (H2O_array(i + 1) - H2O_array(i - 1))/(2*dx);
        d_CO2_array(i) = (CO2_array(i + 1) - CO2_array(i - 1))/(2*dx);
        d2_H2O_array(i) = (H2O_array(i + 1) - 2 * H2O_array(i) + H2O_array(i - 1))/(dx^2);
        d2_CO2_array(i) = (CO2_array(i + 1) - 2 * CO2_array(i) + CO2_array(i - 1))/(dx^2);
    end

    %Diffusion happens
    for i = 2 : nnodes-1
        %Diffuse H2O
        H2O_array(i) = (dD_H2O(i) * d_H2O_array(i) + D_H2O(i) * d2_H2O_array(i)) * dt + H2O_ar
ray(i);
        %Diffuse CO2
        CO2_array(i) = (dD_CO2(i) * d_CO2_array(i) + D_CO2(i) * d2_CO2_array(i)) * dt + CO2_ar
ray(i);
    end

%time increases by time incriment
time = time + dt;


%Boundary conditions at last node (farthest point from bubble)
H2O_array(nnodes) = H2O_array(nnodes - 1);
CO2_array(nnodes) = CO2_array(nnodes - 1);

%Boundary conditions at node 1
```

```
%1st and 2nd concentrations for H2O and CO2 arrays (mass fraction)
H2O_1_mass_fraction = H2O_array(1)/100;
H2O_2_mass_fraction = H2O_array(2)/100;
CO2_1_mass_fraction = CO2_array(1)/(10^6);
CO2_2_mass_fraction = CO2_array(2)/(10^6);
%1st and 2nd concentrations for H2O and CO2 arrays (moles/m^3)
H2O_1_moles_per_meter_cubed = (H2O_1_mass_fraction * 1000 * basalt_density)/H2O_molecular_mass
;
H2O_2_moles_per_meter_cubed = (H2O_2_mass_fraction * 1000 * basalt_density)/H2O_molecular_mass
;
CO2_1_moles_per_meter_cubed = (CO2_1_mass_fraction * 1000 * basalt_density)/CO2_molecular_mass
;
CO2_2_moles_per_meter_cubed = (CO2_2_mass_fraction * 1000 * basalt_density)/CO2_molecular_mass
;
%H2O and CO2 flux (moles/(m^2 * s))
H2O_flux = D_H2O(1)/1e12 * (H2O_2_moles_per_meter_cubed - H2O_1_moles_per_meter_cubed)/(dx/10^
6);
CO2_flux = D_CO2(1)/1e12 * (CO2_2_moles_per_meter_cubed - CO2_1_moles_per_meter_cubed)/(dx/10^
6);
%moles H2O and CO2 in bubble (mols)
H2O_moles_bubble = (H2O_flux * 4 * pi * radius_meters^2) * dt + H2O_moles_bubble;
CO2_moles_bubble = (CO2_flux * 4 * pi * radius_meters^2) * dt + CO2_moles_bubble;
%calculate new H2O and CO2 vapor phases
H2Ov_i = H2O_moles_bubble/(H2O_moles_bubble + CO2_moles_bubble)*100;
CO2v_i = CO2_moles_bubble/(H2O_moles_bubble + CO2_moles_bubble)*100;

%calculate new H2O and CO2 concentrations at node 1
if P_f == 2000
        H2O_node = 3.85 * 10^-9 * H2Ov_i^5 - 1.10 * 10^-6 * H2Ov_i^4 + 1.18 * 10^-4 * H2Ov_i^3
 - 5.93 * 10^-3 * H2Ov_i^2 + 1.75 * 10^-1 * H2Ov_i;
        CO2_node = 9.8667 * CO2v_i + 7.4644;
    elseif P_f == 1000
        H2O_node = 2.97 * 10^-9 * H2Ov_i^5 - 8.51 * 10^-7 * H2Ov_i^4 + 9.14 * 10^-5 * H2Ov_i^3
 - 4.59 * 10^-3 * H2Ov_i^2 + 1.32 * 10^-1 * H2Ov_i;
        CO2_node = 4.7266 * CO2v_i + 2.5497;
    elseif P_f == 500
        H2O_node = 2.11 * 10^-9 * H2Ov_i^5 - 6.08 * 10^-7 * H2Ov_i^4 + 6.57 * 10^-5 * H2Ov_i^3
 - 3.34 * 10^-3 * H2Ov_i^2 + 9.65 * 10^-2 * H2Ov_i;
        CO2_node = 2.3201 * CO2v_i + 0.9244;
end

%update H2O and CO2 concentrations at node 1
H2O_array(1) = H2O_node;
CO2_array(1) = CO2_node;

%show passing of time in command window
%disp(time);
end
```

Plot Diffusion profiles

```
subplot(2,1,1);
plot(length_array, H2O_array, 'g-', 'LineWidth',2);
ylabel('H2O (wt.%)','FontSize',12);
xlabel('length (um)', 'FontSize', 12);
xlim([0 length]);
```

```
ylim([0 H2O_i]);
subplot(2,1,2);
plot(length_array, CO2_array, 'r-', 'LineWidth',2);
ylabel('CO2 (ppm)','FontSize',12);
xlabel('length (um)', 'FontSize', 12);
xlim([0 length]);
ylim([0 CO2_i]);
```

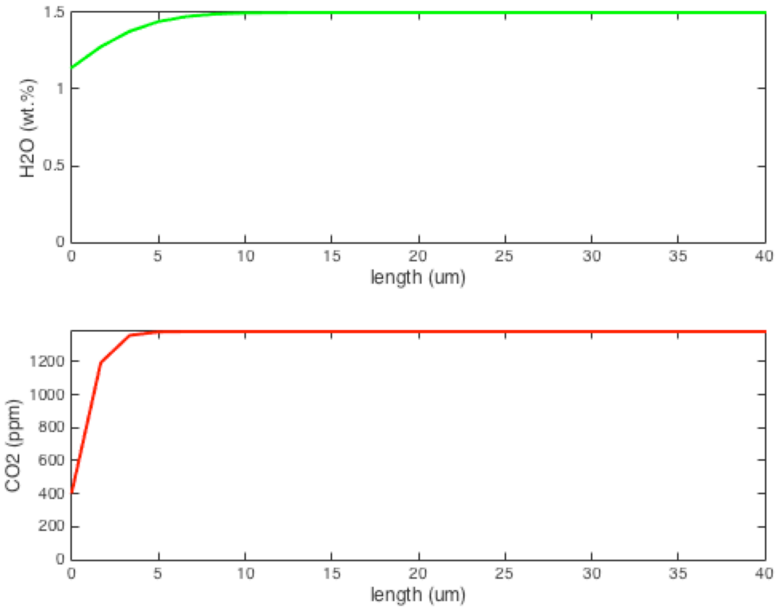

Output Final CO2 and H2O in bubble

```
%output mol fracs
H2O_bubble_mol_percent = H2Ov_i;
CO2_bubble_mole_percent = CO2v_i;
```

Published with MATLAB® R2015a

REFERENCES CITED

Abramoff, M.D., Magalhaes, P.J., Ram, S.J. (2004) Image Processing with ImageJ. *Biophotonics International*, 11 (7), 36-42.

Anderson, A.T. and Brown, G.G. (1993) CO_2 contents and formation pressures of some Kilauean melt inclusions. *American Mineralogist*, 78, 794 – 803.

Bucholz, C.E., Gaetani, G.A., Behn, M.D., Shimizu, N. (2013) Post-entrapment modification of volatiles and oxygen fugacity in olivine-hosted melt inclusions. *Earth and Planetary Science Letters*, 374, 145-155.

Clynne, M.A., and Muffler, L.J.P. (2010) Geologic map of Lassen Volcanic National Park and vicinity, California: U.S. Geological Survey Scientific Investigations Map 2889, scale 1:50,000.

Danyushevsky, L.V., Della-Pasqua, F.N., Sokolov, S. (2000) Re-equilibration of melt inclusions trapped by magnesian olivine phenocrysts from subduction-related magmas: petrological implications. *Contributions to Mineralogy and Petrology*, 138, 68-83.

Danyushevsky, L.V., McNeill, A.W., and Sobolev, A.V. (2002) Experimental and petrological studies of melt inclusions in phenocrysts from mantle-derived magmas: an overview of techniques, advantages, and complications. *Chemical Geology*, 183, 5-24.

Danyushevsky, L.V., and Plechov, P. (2011) Petrolog3: integrated software for modeling crystallization processes. *Geochem. Geophys. Geosyst.*, 12, Q07021, doi:10.1029/2011GC003516.

Dixon, J.E., and Pan, V. (1995) Determination of the molar absorptivity of dissolved carbonate in basanitic glass. *American Mineralogist*, 80, 1339-1342.

Dixon, J.E., Stolper, E.M., Holloway, J.R. (1995) An experimental study of water and carbon dioxide solubilities in mid-ocean ridge basaltic liquids. Part 1: Calibration and solubility models. *Journal of Petrology*, 36, 1607-1631.

Espisoto, R., Bodnar, R.J., Danyushevsky, L.V., De Vito, B., Fedele, L., Hunter, J., Lima, A., Shimizu, N. (2011) Volatile evolution of magma associated with the solchiaro eruption in the phlegrean volcanic district (Italy). *Journal of Petrology*, 52(12), 2431-2460.

Fall, A., Tattitch, B., Bodnar, R.J. (2011) Combined microthermometric and Raman spectroscopic technique to determine the salinity of H_2O-CO_2-NaCl fluid inclusions based on clathrate melting. *Geochemica et Cosmochimica Acta*, 75, 951-964.

Giordano, D., Nichols, A.R.L., Dingwell, D.B. (2005) Glass transition temperatures of natural hydrous melts: a relationship with shear viscosity and implications for the welding process. *Journal of Volcanology and Geothermal Research*, 142, 105-118

Gaetani, G.A., O'Leary, J.A., Shimizu, N., Bucholz, C.E., Newville, M. (2012) Rapid Equilibration of H_2O and oxygen fugacity in olivine-hosted melt inclusions. *Geology*, 40, 915-918.

Gualda, G.A.R., Ghiorso, M.S., Lemons, R.V., Carley, T.L. (2012) Rhyolite-METLS: A modified calibration of MELTS optimized for silica-rich, fluid-bearing magmatic systems. *Journal of Petrology*, 53, 875-890.

Hauri, E. (2001) Sims analysis of volatiles in silicate glasses, 2: isotopes and abundances in Hawaiian melt inclusions. *Chemical Geology*, 183, 115-141.

Iacono-Marziano, G., Morizet, Y., Le Trong, E., Gaillard, F. (2012) New experimental data and semi-empirical parameterization of H_2O-CO_2 solubility in mafic melts. *Geochimica et Cosmochimica Acta*, 97, 1-23.

Johnson, E.R., Wallace, P.J., Cashman, K.V., Delgado Granados, H., Kent, A.J.R. (2008) Magmatic volatile contents and degassing-induced crystallization at Volcano Jorullo, Mexico: implications for melt evolution and the plumbing systems of monogenetic volcanoes. *Earth Planet. Sci. Lett.*, 269, 477-486.

Johnson, E.R., Wallace, P.J., Granados, H.D., Manea, V.C., Kent, A.J.R., Bindeman, I.N., Donegan, C.S. (2009) Subduction-related volatile recycling beneath Central Mexico: insights from melt inclusions, oxygen isotopes, and geodynamic models. *J. Petrol.*, 50, 1729-1764.

Kumazawa, M. and Anderson, O.L. (1969) Elastic moduli, pressure derivatives, and temperature derivatives of single-crystal olivine and single-crystal forsterite. *J. Geophys. Res.*, 74, 5961-5972.

Lange, R., L. and Carmichael, I.S.E. (1990) Thermodynamic properties of silicate liquids with emphasis on density, thermal expansion, and compressibility. Reviews in Mineralogy, 24, 25-59.

Lloyd, A.S., Plank, T., Ruprecht, P., Hauri, E.H., Rose, W. (2012) Volatile Loss from Melt Inclusions in Pyroclasts of Differing Sizes. *Contributions to Mineralogy and Petrology* 165(1), 129–53.

Lloyd, A.S., Ruprecht, P., Hauri, E.H., Rose, W., Gonnermann, H.M., Plank, T. (2014) NanoSIMS results from olivine-hosted melt embayments: magma ascent during explosive basaltic eruptions. *Journal of Volcanology and Geothermal Research*, 283, 1- 18.

Lowenstern, J.B. (1995) Application of silicate-melt inclusions to the study of magmatic volatiles. *In* Magmas, fluids and ore deposits. Thompson, J.F.H. (ed), 71-100.

Luhr, J.F. (2001) Glass inclusions and melt volatile contents at Paricutin Volcano, Mexico. *Contributions to Mineralogy and Petrology*, 142, 261-283.

Metrich, N., and Wallace, P.J. (2008) Volatile abundances in basaltic magmas and their degassing paths tracked by melt inclusions. *Minerals, Inclusions, and Volcanic Processes*, Reviews in Mineralogy and Geochemistry, Mineralogical Society of America, 69, 363-402.

Moore, L.R., Gazel, E., Tuohy, R., Lloyd, A.S., Esposito, R., Steele-Macinnis, M., Hauri, E.R., Wallace, P.J., Plank, T., Bodnar, R.J. (2015) Bubbles matter: An assessment of the contribution of vapor bubbles to melt inclusion budgets. American Mineralogist, 100(4), 806-823.

Newman, S., Lowenstern, J.B. (2002) VolatileCalc: a silicate melt-H_2O-CO_2 solution model written in Visual Basic for Excel. *Computers and Geosciences*, 28(5), 597-604.

Nichols, a. R.L. & Wysoczanski, R.J. (2007) Using micro-FTIR spectroscopy to measure volatile contents in small and unexposed inclusions hosted in olivine crystals. *Chemical Geology*, 242(3-4), 371–384.

Papale, P., Moretti, R., Barbato, D. (2006) The compositional dependence of the saturation surface of $H_2O + CO_2$ fluids in silicate melts. *Chemical Geology*, 229, 78-95.

Riker, J. (2005) The 1859 eruption of Mauna Loa Volcano, Hawaii: Controls on the development of long lava channels. Unpublished M.S. Thesis, University of Oregon.

Roedder, E. (1979) Origin and significance of magmatic inclusions. *Bulletin de Mineralogie*, 102, 467-510.

Sorby, H.C. (1858) On the microscopic structure of crystals, indicating the origin of minerals and rocks. *Geol. Soc. London Quart. Jor.*, 14(1), 453-500.

Suzuki, I. (1975) Thermal expansion of periclase and olivine, and their anharmonic properties. *J. Phys. Earth*, 23,145-159.

Steele-MacInnis, M., Esposito, R., and Bodnar, R.J., (2011) Thermodynamic model for the effect of post-entrapment crystallization on the H_2O-CO_2 systematics of vapor-saturated, silicate melt inclusions. *Journal of Petrology*, 52, 2461-2482.

Wallace, P.J., Kamenetsky, V.S., Cervantes, P. (2015) Melt inclusion CO2 contents, pressures of olivine crystallization, and the problem of shrinkage bubbles. *American Mineralogist*, 100(4), 787-794.

Wright R.B., and Wang, C.H. (1973) Density effect on the Fermi resonance in gaseous CO_2 Raman scattering. *J. Chem. Phys.*, 58, 2893-2895.

Wright R.B. and Wang, C.H. (1975) Effect of density on the Raman scattering of molecular fluids. II. Study of intermolecular interactions in CO_2. *J. Chem. Phys.*, 61, 2707-2710.

Wysoczanski, R. & Tani, K. (2006) Spectroscopic FTIR imaging of water species in silicic volcanic glasses and melt inclusions: An example from the Izu-Bonin arc. *Journal of Volcanology and Geothermal Research*, 156(3-4), 302–314.